# Mineralium Deposita

# Discovery of Ni-smectite rich saprolite at Loma Ortega, Falcondo mining district (Dominican Republic): geochemistry and mineralogy of an unusual case of "hybrid hydrous Mg silicate - clay silicate" type Ni-laterite

--Manuscript Draft--

| | |
|---|---|
| **Manuscript Number:** | |
| **Full Title:** | Discovery of Ni-smectite rich saprolite at Loma Ortega, Falcondo mining district (Dominican Republic): geochemistry and mineralogy of an unusual case of "hybrid hydrous Mg silicate - clay silicate" type Ni-laterite |
| **Article Type:** | Regular Articles |
| **Corresponding Author:** | Cristina Villanova-de-Benavent, Ph.D<br>Universitat de Barcelona<br>Barcelona, SPAIN |
| **Corresponding Author Secondary Information:** | |
| **Corresponding Author's Institution:** | Universitat de Barcelona |
| **Corresponding Author's Secondary Institution:** | |
| **First Author:** | Esperança Tauler |
| **First Author Secondary Information:** | |
| **Order of Authors:** | Esperança Tauler |
| | John Frederick Lewis |
| | Cristina Villanova-de-Benavent, Ph.D |
| | Thomas Aiglsperger |
| | Joaquín Antonio Proenza |
| | Cristina Domènech |
| | Tamara Gallardo |
| | Francisco Longo |
| | Salvador Galí |
| **Order of Authors Secondary Information:** | |
| **Funding Information:** | Secretaría de Estado de Investigación, Desarrollo e Innovación (CGL2009-10924) — Dr Joaquín Antonio Proenza<br>Secretaría de Estado de Investigación, Desarrollo e Innovación (CGL2012-36263) — Dr Joaquín Antonio Proenza |
| **Abstract:** | Hydrous Mg silicate-type Ni-laterite deposits, like those in the Falcondo district, Dominican Republic, are dominated by Ni-enriched serpentines and garnierites. Recently, abundant Ni-smectites in the saprolite zone have been discovered in Loma Ortega, one of the nine Ni-laterite deposits in Falcondo. A first detailed study on the Ni-smectites has been performed (µXRD, SEM, EMP), in addition to a geochemical and mineralogical characterization of the Loma Ortega profile (XRF, ICP-MS, XRD). Unlike other smectite occurrences in laterite profiles worldwide, the Loma Ortega smectites are trioctahedral and exhibit high Ni contents never reported before. These Ni-smectites may be formed from weathering of pyroxene and olivine, and their composition can be explained by the mineralogy and the lithology of the Al-depleted, olivine-rich parent ultramafic rock. In accordance, we propose the classification of "hybrid hydrous Mg silicate - clay silicate" type Ni-laterite deposit for Loma Ortega. Our study shows that Ni-laterites are mineralogically complex, and that a hydrous Mg |

| | |
|---|---|
| | silicate ore and a clay silicate ore can be confined to the same horizon in the weathering profile, which has significant implications from a recovery perspective. |
| **Suggested Reviewers:** | Anne Gaudin<br>Université de Nantes<br>Anne.Gaudin@univ-nantes.fr<br>Given her extended expertise on Ni-bearing smectites found on Ni-laterite profiles in Murrin Murrin, Australia. Her works have been cited many times in the submitted paper. |
| | Martin A Wells<br>CSIRO<br>martin.wells@csiro.au<br>For his knowledge on hydrous Mg silicate-type Ni-laterite deposits. |
| | Sarah A Gleeson<br>University of Alberta<br>Sgleeson@ualberta.ca<br>For her works on Ni-laterite deposits in Cerro Matoso (Colombia) and in Cameroon. |

# Discovery of Ni-smectite rich saprolite at Loma Ortega, Falcondo mining district (Dominican Republic): geochemistry and mineralogy of an unusual case of "hybrid hydrous Mg silicate – clay silicate" type Ni-laterite

Esperança Tauler[1], John F. Lewis[2], Cristina Villanova-de-Benavent[1*], Thomas Aiglsperger[1], Joaquín A. Proenza[1], Cristina Domènech[1], Tamara Gallardo[1], Francisco Longo[3], Salvador Galí[1]

[1]*Departament de Cristal·lografia, Mineralogia i Dipòsits Minerals, Universitat de Barcelona (UB), Martí i Franquès s/n, 08028 Barcelona, Spain*

**Corresponding author, e-mail: cvillanovadb@ub.edu*

[2]*Department of Earth and Environmental Sciences, The George Washington University, 20052 Washington D.C., USA*

[3]*Faculty of Engineering, Universidad Católica Tecnológica del Cibao (UCATECI), Ave. Universitaria esq. Ave. Pedro Rivera, PO Box 401, La Vega, Dominican Republic*

## Abstract

Hydrous Mg silicate-type Ni-laterite deposits, like those in the Falcondo district, Dominican Republic, are dominated by Ni-enriched serpentines and garnierites. Recently, abundant Ni-smectites in the saprolite zone have been discovered in Loma Ortega, one of the nine Ni-laterite deposits in Falcondo. A first detailed study on the Ni-smectites has been performed (µXRD, SEM, EMP), in addition to a geochemical and mineralogical characterization of the Loma Ortega profile (XRF, ICP-MS, XRD). Unlike other smectite occurrences in laterite profiles worldwide, the Loma Ortega smectites are trioctahedral and exhibit high Ni contents never reported before. These Ni-smectites may be formed from weathering of pyroxene and olivine, and their composition can be explained by the mineralogy and the lithology of the Al-depleted, olivine-rich parent ultramafic rock. In accordance, we propose the classification of "hybrid hydrous Mg silicate – clay silicate" type Ni-laterite deposit for Loma Ortega. Our study shows that Ni-laterites are mineralogically complex, and that a hydrous Mg silicate ore and a clay silicate ore can be confined to the same horizon in the weathering profile, which has significant implications from a recovery perspective.

**Keywords**

Ni-smectite, Ni-laterite, hydrous Mg silicate deposit, clay silicate deposit, Dominican Republic

## Introduction

Nickel laterite deposits are regoliths derived from the chemical weathering of ultramafic rocks, containing economically exploitable concentrations of Ni±Co. Several authors recognized that interactions between the composition of the protolith, tectonic setting, geomorphology, topography, drainage, chemistry of groundwater and organic matter, climate and weathering rates control the enrichment processes within lateritic weathering profiles (e.g. Trescases 1975; Golightly 1981, 2010; Elias et al. 1981; Gleeson et al. 2003; Freyssinet et al. 2005). Geographically, Ni-laterites are observed within 26 degrees of the equator, indicating the influence of tropical climate conditions (Butt and Cluzel 2013 and references therein).

Ni(±Co)-laterite deposits account for about 40% of the current world's annual Ni production and host over 60% of the world land-based Ni resources (Gleeson et al. 2003; Kuck 2013). In addition, Ni-laterites are considered targets for critical metals exploration as Sc and Platinum Group Elements (PGE) (Aiglsperger et al. 2015, 2016). The Caribbean region, particularly Cuba and the Dominican Republic, contains about 10% of world’s resources of Ni lateritic deposits (Dalvi et al. 2004; Nelson et al. 2011).

In general, three subtypes of Ni±Co laterites profile can be distinguished according to their main laterite architecture as well as by their dominant Ni-bearing mineralogy (Brand et al. 1998; Elias 2002; Freyssinet et al. 2005; Butt and Cluzel 2013): a) oxide deposits dominated by Fe oxyhydroxides  forming a ore mineral horizon at the pedolith-saprolite boundary; b) hydrous Mg silicate deposits dominated by hydrated Mg-Ni silicates (mainly Ni-serpentine and garnierite) occurring deep in the saprolite; c) clay silicate deposits dominated by smectitic clays (e.g. nontronite) commonly occurring in the upper saprolite or pedolith. The hydrous Mg silicate deposits generally have the highest Ni grade (1.8–2.5 wt.% Ni) and are characterised by a thick serpentine-dominated saprolite horizon covered by a relatively thin Fe-oxyhydroxide-dominated limonite horizon (laterite sensu stricto horizon). These deposits are formed under conditions of a low water table and continuous tectonic uplift (Butt and Cluzel 2013; Freyssinet et al. 2005).

The Dominican Republic has been an important producer of Ni from saprolite ore since 1968 when the Falcondo plant went into production (Nelson et al. 2011). Falcondo is the largest hydrous Mg silicate-type Ni-laterite district of the Caribbean region (Lewis et al. 2006), draws ore from nine deposits and contains measured and indicated Ni resources of 67.8 Mt at a grade of 1.5 % Ni and 4.9 Mt of inferred resources at 1.4 % Ni (Redwood 2014). The Loma Ortega deposit, in the northwestern part of the Falcondo district, is one of the strategic areas under exploration at this time (Fig. 1). Despite the importance of this deposit, no previous investigations have been carried out on the mineralogy, geochemistry, and origin. In addition, this ore deposit gained interest due to the discovery of Ni-smectites in the saprolite zone during recent mining activities.

In this contribution, we report the first results of a mineralogical and geochemical investigation of the Loma Ortega Ni-laterite profile, aiming at reporting the first data concerning the presence of a Ni-smectite rich laterite profile (typical of clay silicate-type Ni-laterites) in the Falcondo mining district, traditionally interpreted as a hydrous Mg silicate-type Ni-laterite.

We interpret the mineralogical and the geochemical evolution of the Loma Ortega profile from representative fragments picked along a core provided by Falcondo Glencore Xstrata Nickel (now Americano Nickel-Falcondo). Samples were investigated using X-ray fluorescence (XRF), ICP mass spectrometry (ICP-MS), optical microscopy, X-ray diffraction (XRD), X-ray microdiffraction, scanning electron microscopy (SEM) and electron microprobe analysis (EMP).

## Geological setting

The Falcondo district is developed on the Loma Caribe peridotite, which occurs as a linear belt of ultramafic rocks in Central Hispaniola (Fig. 1). Loma Caribe forms the core of the Median Belt (Lewis and Draper 1990), a remarkable association of the oldest island arc rocks in the northern Caribbean along with oceanic plateau rocks (Lewis et al. 2000; Kesler et al. 2005; Escuder-Viruete et al. 2010; Torró et al. 2016). These ophiolite-related peridotites, loosely described as serpentinized peridotite, crop out as isolated bodies in suture zones along the northern margin of the Caribbean Plate (Lewis and Draper 1990; Lewis et al. 2006). The Loma Caribe peridotite is mainly composed of lherzolite, clinopyroxene-bearing harzburgite, harzburgite, orthopyroxene-bearing dunite and dunite (Lewis et al. 2006; Proenza et al. 2007; Marchesi et al. 2016). Dunite bodies are small and show sharp contacts with the harzburgites. In addition, small, lens-like shaped chromitite bodies are enclosed in dunites and serpentinites (Proenza et al. 2007). Peridotites are locally intruded by dykes of gabbro of Barremian age (~125 Ma), and of dolerite with geochemical affinities of E-MORB, N-MORB and back-arc basin basalts (Escuder-Viruete et al. 2008). The emplacement of peridotite towards the N-NE onto early Cretaceous island arc volcanic rocks (Maimón and Los Ranchos Formations) occurred in the Aptian-Albian along a thrust fault that was later reactivated in the Middle Eocene (Draper et al. 1996).

The peridotites typically show porphyroclastic textures with strongly deformed orthopyroxene crystals. The Cr# in spinel from Loma Caribe peridotites varies from 0.30 (lherzolite) to 0.88 (dunite). Compositions of accessory spinel from dunites and harzburgites resemble those from supra-subduction zone mantle peridotites, whereas compositions of spinel from lherzolites are similar to those of abyssal peridotites (Lewis et al. 2006; Proenza et al. 2007).

Loma Caribe peridotites were interpreted by Lewis et al. (2006) as fragments of Jurassic-Cretaceous Pacific oceanic lithosphere that had been modified in a supra-subduction zone environment related to the early Cretaceous Caribbean arc, which was affected by a mantle plume (Duarte plume). In contrast, according to Marchesi et al. (2016), major element concentrations support the idea that the protoliths of Loma Caribe peridotites mostly melted at 1-2 GPa, as in ocean ridge and subduction zone mantle contexts. These authors interpret that the compositional variability of the Loma Caribe peridotite reflects different stages of generation of suboceanic mantle lithosphere during the Lower Cretaceous initiation of subduction beneath the Caribbean arc.

Lateritization began in the early Miocene, when serpentinized peridotites were exposed to weathering and erosion (Lewis et al. 2006 and references therein). Haldeman et al.

(1979) recognized at least four physiographic cycles from different surface levels and benches on hill slopes. The lateritization process continues today, although the optimum conditions for lateritization may not have been continuous since the early Miocene.

### The lateritic profiles at the Falcondo mining district

The Falcondo mining district is divided into nine ore deposits, from west to east: Loma Ortega, Loma Miranda, Loma Caribe, Loma Guardarraya, Loma Fraser, Loma Larga, Loma Taína, Loma Peguera and Loma Cumpié (Fig. 1) (Haldemann et al. 1979; Lithgow 1993; Lewis et al. 2006; Villanova-de-Benavent et al. 2014).

The weathering profile in Falcondo includes, from bottom to top: i) peridotite parent rock, ii) lower or hard saprolite, iii) upper or soft saprolite, iv) lower limonite, v) upper limonite and vi) duricrust or ferricrete. The thickness of the different zones in the profile varies vertically and laterally. In general, the weathering horizons are erratically developed and complete profiles are extremely rare (Lewis et al. 2006; Aiglsperger et al. 2015, 2016). The laterite profile is almost entirely saprolitic (the saprolite horizon is up to 40 m thick), with only a thin silicified ferruginous zone (up to 10 m thick). In several areas of the deposit the limonite zone *sensu stricto* is totally eroded. The main Ni ores are Ni-bearing serpentines that form the bulk of the saprolite, and "garnierites" (Mg-bearing Ni-phyllosilicates) that occur mostly as veins and fracture coatings concentrated in the lowermost part of the saprolite horizon, toward the base of the profile (Lewis et al. 2006; Tauler et al. 2009; Villanova-de-Benavent et al. 2014, 2016).

## Sampling and analytical techniques

### Sampling

The Ni-laterite profile of Loma Ortega was studied from a 41.3 m long drill core (coded O954-0307) provided by Falcondo Glencore Xstrata Nickel in 2007. The location of the core is easting 340800 and northing 2118900, at an elevation of 367 m, in an area with abundant vegetation (Fig. 1). Four zones can be distinguished in the core (from bottom to top): i) serpentinized peridotite protolith, ii) lower saprolite, iii) upper saprolite (also called “ore zone”), and iv) silicified ferruginous saprolite (Fig. 2). For the present work major and trace elements were analysed from eighty-two samples, from which twenty-two were selected as representative of the four zones identified.

## Analytical techniques

Major element compositions were determined at the Actlabs Laboratories (Ontario, Canada) by XRF (Table 1). Precision was better than ±1.5 wt.% for a concentration of ≥10 wt.% and ±2 wt.% for a concentration ≤10 wt.%.

PGE contents were obtained at Genalysis Ltd. (Maddington, Western Australia) by ICP-MS after nickel sulfide fire assay collection following the method described by Chan and Finch (2001). The detection limits were 1 ppb for Rh and 2 ppb for Os, Ir, Ru, Pt and Pd.

XRD data were collected with a Panalytical X’Pert PRO MPD X-ray diffractometer with monochromatized incident Cu $K\alpha1$ radiation at 45 kV and 40 mA, and equipped with a PS detector with amplitude of 2.113° (Centres Científics i Tecnològics, Universitat de Barcelona). The patterns were obtained by scanning random powders from 4° to 80° ($2\theta$) on samples crushed in an agate mortar to a particle size below 40 μm. Two data sets were obtained with different conditions: a) a scan time of 300 seconds at a step size of 0.017° ($2\theta$) and a fixed divergence slit of 0.25°, b) a scan time of 50 seconds at a step size of 0.017° ($2\theta$) and variable divergence slit. The patterns of samples on oriented mounts were collected as follows: i) air-dry, scanning from 2° to 80° ($2\theta$); ii) on samples saturated with ethylene glycol and scanning from 2° to 30° ($2\theta$) and iii) by heating the same sample up to 550° C and scanning from 2° to 30° ($2\theta$), at a step size of 0.017° and scan time of 50 seconds. Mineral identification and semi quantitative results were facilitated using the *X’Pert Highscore* search-match software with Powder Diffraction File, version 2 from JCPDS. Quartz, when present in the sample, was used as an internal standard to correct diffraction patterns for instrumental shifts in $2\theta$ position. Quantitative mineral phase analyses were obtained by full profile Rietveld refinement using powder diffraction data. The software used was TOPAS version 4.2.

Mineral phases and textural features were examined on polished thin sections and polished probes under an optical microscope using both transmitted and reflected light, and under a SEM Quanta 200 FEI, XTE 325/D8395, coupled to an INCA Energy Dispersive Spectrometer (EDS) 250 EDS microanalysis system with the operating conditions of 20 kV and 5 nA (Centres Científics i Tecnològics, Universitat de Barcelona).

EMP analyses were performed over selected areas on several representative polished thin sections and polished sections, with a four-channel CAMECA SX50 EMP. The analytical conditions were 20 kV accelerating voltage, 10 nA beam current, 2 μm beam diameter, and counting time of 10 seconds per element (Centres Científics i Tecnològics, Universitat de Barcelona). Calibrations were performed using natural and synthetic reference materials: hematite (Fe, LIF, Kα), rutile (Ti, PET, Kα), periclase (Mg, TAP, Kα), rhodonite (Mn, LIF, Kα), $Al_2O_3$ (Al, TAP, Kα), $Cr_2O_3$ (Cr, PET, Kα), metallic vanadium (V, LIF, Kα), diopside (Si, TAP, Kα), NiO (Ni, LIF, Kα), wollastonite (Ca, PET, Kα), albite (Na, TAP, Kα), orthoclase (K, PET, Lα), metallic cobalt (Co, LIF, Kα).

The structural formulae of olivine, pyroxene and serpentine were calculated on the basis of 8, 6 and 7 oxygens, respectively. The formulae of garnierite and smectite were calculated using 11 oxygens. Fe was considered as $Fe^{2+}$ in olivine, pyroxene and primary serpentine, and as $Fe^{3+}$ in secondary serpentine, garnierites, smectites and asbolanes.

Microdiffraction measurements in Ni-smectite were made using a Bruker-AXS D8-Discover instrument (Universitat Rovira i Virgili), equipped with a vertical θ-θ goniometer, parallel incident beam (Göbel mirror), XYZ motorized stage and a GADDS (General Area Diffraction System) detector. The area of interest in the polished thin section was selected with the aid of a video-laser focusing system. An X-ray collimator allowed analyzing areas of 500 μm. The X-ray diffractometer was operated at 40 kV and 40 mA to generate CuKα radiation. One frame (2D XRD patterns) covering 2-21° (2θ) taken at a distance of 15 cm from the sample was measured. The exposition time was of 900s per frame and the two dimensional data was Chi-integrated to generate the conventional 2θ versus intensity diffractogram. Identification of the minerals was achieved by comparison of the XRD diffractogram with the ICDD data base (2007 release) using *Diffrac plus Evaluation* software (Bruker 2007).

## Results

### Whole-rock geochemistry

Figure 2 shows the general geochemical trend within the laterite profile from drill core O954-0307 with respect to the distribution of major elements (Si, Al, Fe and Mg), Ni and PGE. In general MgO and $SiO_2$ are dominant throughout the profile with average values of ~30 and ~45 wt.%, respectively. However, both elements follow mirror inverted tendencies as clearly seen in one anomaly close to the surface where MgO drops to concentrations down to ~2 wt.% and $SiO_2$ reaches concentrations of ~70 wt.% (Fig. 2). However, a characteristic Mg discontinuity with values lower than 1 wt.% MgO as previously reported from Ni-laterites from the Falcondo mining disctrict is not observed (Aiglsperger et al. 2016). In addition $Al_2O_3$ and $Fe_2O_3$ show rather constant tendencies within the drill core with average concentrations of ~1 wt.% and ~11 wt.%, respectively (Fig. 2). A slight $Fe_2O_3$ enrichment trend with contents of up to ~18 wt.% is observed at ~2.5 m towards the surface.

Ni concentrations are low (~0.5 %) from bottom to ~18 m and near the surface. However, a well defined ore zone with concentrations up to ~3 % Ni (average 1.8 % Ni) is developed from ~18 m to ~2.5 m (Fig. 2).

Total PGE concentrations range from 25 ppb at the bottom of the drill core to 75 ppb within the upper part of the ore zone (5 m) (Fig. 2; Table 2). In general, individual PGE follow similar trends with constant, lower concentrations up to the central part of the ore zone (11 m) and highest values at 5 m with a subsequent decrease towards the surface. Ru and Pt are the most abundant PGE, however, it is important to note that Pt concentrations are nearly stable from 5 m to 0.5 m (21 and 20 ppb, respectively), whereas Ru concentrations drop from 21 ppb to 9 ppb (Fig. 2). As a consequence IPGE (Os, Ir, Ru) to PPGE (Rh, Pt, Pd) ratios change from 1.59 (upper ore zone) to 0.81 at highest levels (Table 2). Chondrite-normalized PGE patterns reveal rather similar flat PGE trends for all samples as previously observed in Ni-laterites from the Falcondo mining district (Fig. 3). With the exception of the highest samples at 0.5 m Ru shows a general positive anomaly for all samples. Pt on the other hand has either a positive trend (at 35 m, 28 m and 0.5 m), a slightly negative trend (at 11 m and 8 m) or an even trend (at 5 m).

## Mineralogy and textures

The mineralogy of selected samples representative of the protolith, the saprolite zone and the ferruginous silicified saprolite, obtained by powder XRD, is displayed in Figs. 4 and 5. The characteristic textural features of the protolith and the saprolite are presented in Figs. 6 and 7, respectively. In particular, Fig. 8 displays the mineralogy and textural relationships between Ni-smectites and olivine, pyroxene and serpentine II. Finally, the petrography of the silicified ferruginous saprolite is shown in Fig. 9. The mineralogy and mineral chemistry of the Ni-bearing phases of the ore zone is depicted in Figs. 10 (Ni-serpentine), 11 (garnierite) and 12 (Ni-smectite). A selection of EMP analyses of primary and secondary phases is included in Tables 3 to 6.

### Protolith

The primary ultramafic rock consists of serpentinized harzburgite and serpentinite.

The serpentinite is found at the bottom of the core until a depth of 24 m (Fig. 4). It is grey-green in color and shows slight weathering, limited to fracture planes (Fig. 5a). Different generations of fine veins are found, some of them filled by silica. According to powder XRD, the bulk rock is made up by serpentine (96 wt.%), mainly lizardite and minor chrysotile, with less abundant goethite (2 wt.%), maghemite (1 wt.%) and hematite (1 wt.%) (Figs. 4, 5a). Under the optical microscope the serpentine appears highly foliated (Fig. 6a).

Relicts of serpentinized harzburgite are mainly found at depths between 16 and 24 m, in the lower saprolite zone, and are dark green in color (Fig. 5b). They consist of olivine, pyroxene (enstatite and diopside), serpentine and minor Cr-spinel (Figs. 4, 5b). According to the observations under optical and scanning electron microscope, olivine grains are encircled by serpentine in a mesh texture arrangement and coexist with pyroxene (Fig. 6b). Diopside is intergrown with olivine (Fig. 6c) and with enstatite (Fig.

6d), frequently showing irregular boundaries due to its replacement by serpentine (Fig. 6c). Diopside also occurs as exsolution lamellae parallel to cleavage in subhedral enstatite porphyroclasts (Fig. 6e).

The composition of olivine, enstatite and diopside is presented in Table 3. Olivine has a $Fo_{90}$ [(Mg/Mg+$Fe^{2+}$)·100] (average of 12 analyses) and a Ni content of 0.40 wt.% NiO (0.02 apfu Ni). Enstatite is characterized by a $En_{89}$ [(Mg/Ca+Mg+$Fe^{2+}$)·100], a $Wo_2$ [(Ca/Ca+Mg+$Fe^{2+}$)·100], and Ni content lower than that of olivine (0.05 wt.% NiO, 0.002 apfu Ni, average of 10 analyses). Diopside contains 0.03 wt.% NiO (0.001 apfu Ni) and may have significant Cr contents (0.75 wt.% $Cr_2O_3$, 0.02 apfu Cr, average of 12 analyses) (Table 3).

Cr-spinel is detected all across the core, and is usually well preserved in the saprolite and in the silicified ferruginous saprolite (Fig. 6f). Its chemical composition is rather homogeneous along the core. In all cases, only the nuclei of the grains appear unaltered, yielding an average of 62.13 wt.% $Cr_2O_3$, 5.86 wt.% $Al_2O_3$, 21.63 wt.% FeO, 1.62 wt.% $Fe_2O_3$ and 6.84 wt.% MgO (average of 7 analyses) (Fig. 6f). The Cr# [Cr/(Cr+Al)] varies between 0.87 and 0.90 and Mg# [Mg/(Mg+$Fe^{2+}$)] ranges from 0.44 to 0.50, which corresponds to the compositional range of Cr-spinels found in dunites from the Loma Caribe peridotite belt (Proenza et al. 2007; Marchesi et al. 2016). In contrast, the thin rims of the Cr-spinel grains are mostly formed by Fe oxides (66.23 wt.% $Fe_2O_3$, 30.09 wt.% FeO) with very low Cr (1.24 wt.% $Cr_2O_3$) (Fig. 6f).

The chemical composition of the serpentines from the protolith (serpentinite and harzburgite), hereafter referred to as serpentine I, is given in Table 4. On one hand, the serpentine from the serpentinized peridotite has a very low Al content (below 0.73 wt.% $Al_2O_3$, <0.09 apfu Al), and its Ni and Fe contents range from 0.15 to 0.53 wt.% NiO (0.01-0.02 apfu Ni) and from 1.37 to 1.87 wt.% FeO (0.06-0.08 apfu Fe). The average structural formula is $(Mg_{2.72}Fe^{2+}_{0.07}Ni_{0.02}Cr_{0.01})(Si_{2.08}Al_{0.01})O_5(OH)_4$ (11 analyses). On the other hand, the serpentine I from the harzburgite can be divided into three groups according to the chemical composition. In the first group Al is low (<0.02 wt.% $Al_2O_3$, <0.002 apfu Al) and Ni and Fe vary from 0.25 to 0.46 wt.% NiO (0.01-0.02 apfu Ni) and from 4.41 to 7.62 wt.% FeO (0.18-0.33 apfu Fe). In the second group Al is slightly higher (up to 0.14 wt.% $Al_2O_3$, 0.02 apfu Al), Ni is systematically below 0.29 wt.% NiO (0.01 apfu Ni) and Fe is comparable to that of the first group (2.48-7.12 wt.% FeO, 0.10-0.30 apfu Fe). The serpentines from the third group contain the lowest Ni (<0.05

wt.% NiO, <0.002 apfu Ni) and Fe (2.80 wt.% FeO, 0.11 apfu Fe) and the highest Al (1.20-1.48 wt.% Al2O3, 0.13-0.16 apfu Al) and Ca (0.15-0.52 wt.% CaO, 0.01-0.03 apfu Ca) contents. The average structural formula of the first group is $(Mg_{3.04}Fe^{2+}_{0.10}Ni_{0.02})(Si_{1.84}Fe^{2+}_{0.16})O_5(OH)_4$ (6 analyses), that of the second group is $(Mg_{2.80}Fe^{2+}_{0.17}Ni_{0.003})(Si_{2.00}Al_{0.01})O_5(OH)_4$ (8 analyses) and that of the third group is $(Mg_{2.67}Fe_{0.11}Ni_{0.001}Ca_{0.017}Al_{0.15})Si_{1.98}O_5(OH)_4$ (2 analyses).

The Ni content in the first group of serpentines is similar to that observed in olivine, and this may indicate that these serpentines formed after olivine. However, the low Ni but significant Al contents in the second group of serpentines suggest that they formed after enstatite. Finally, according to the high Al and Ca contents, the third group may have formed from diopside. All these serpentines I are products of hydrothermal alteration of the primary ultramafic rock under deep oceanic conditions, prior to weathering.

### Saprolite zone

The saprolite zone is intersected between 24 and 3 m in depth, and can be divided into: i) lower saprolite (24-18 m) and ii) upper saprolite or "ore zone" (18-2.5 m) (Fig. 4). The lower saprolite is made up by hard, dark grey harzburgite or serpentinite fragments with a brown to orange alteration rim, surrounded by a yellowish, soft, clayey material (Fig. 5b). According to powder XRD, the lower saprolite consists of 50 wt.% serpentine, 41 wt.% olivine, 6 wt.% pyroxene and 2 wt.% maghemite (Figs. 4, 5b). In the upper saprolite, the rocky fragments are brown to orange or ochre and are smaller and more friable than in the lower saprolite (Fig. 5c), and the soft clayey material is more abundant. The upper saprolite is made up by 67 wt.% serpentine, 16 wt.% goethite, 8 wt.% quartz, 5 wt.% olivine, 2 wt.% maghemite and 1 wt.% pyroxene (Figs. 4, 5c). At shallower depths, the saprolite fragments are orange to ochre (Fig. 5d), and primary minerals such as olivine and pyroxene are not detected. The rock consists mostly of serpentine (lizardite), less abundant maghemite, goethite and quartz (Fig. 5d). Under the optical microscope the saprolite displays a mesh texture similar to that of the serpentinized protolith, although the olivine fragments have been completely replaced by brownish, silicified Fe oxyhydroxide aggregates (goethite), surrounded by a yellowish serpentine vein framework (Figs. 7a-b). Different shades of grey in the BSE images reveal different serpentines in the framework, ones with higher Ni than the others (Fig. 7c).

Mn-Co-Ni-phases (asbolanes) are present as coatings or vein infillings, coexisting with quartz, goethite and serpentine II and are found to replace pyroxene, olivine and serpentine along grain boundaries and fractures (Fig. 7d).

Green micrometer to centimeter-sized garnierite veinlets are common along the upper saprolite horizon. Garnierite is pale green in color and is often associated with greenish white, translucent quartz (Fig. 7e). The study under optical and electron microscopy reveals banded botryoidal features. The botryoidal aggregates are surrounded by a cryptocrystalline quartz matrix (Fig. 7f-g).

Smectite was detected by powder X-ray diffraction between 16.7 and 7.2 m in depth (Figs. 4 and 5c, d), and occurs as millimeter-sized, irregularly distributed aggregates (Fig. 8). *In situ* X-ray microdiffraction was carried out on one thin section previously analyzed by EMP. The most intense spacings are 13.5 Å and 7.24 Å corresponding to smectite and lizardite respectively. The 13.5 Å spacing is lower than the 14.4 Å spacing of the Ni-bearing saponite reported by Decarreau et al. (1987), probably due to instrumental effects in X-ray microdiffraction (Fig. 8a). In addition, oriented mounts of a volume of sample including smectite and lizardite show a peak at 14.8 Å which expands to 16.6Å after glycolation and contracts to about 9.7Å on heating at 550ºC (Fig. 8b). This swallowing behavior confirms the presence of smectite. The 7.29 Å peak, which corresponds to lizardite, remains unaltered after these treatments. The presence of lizardite in the sample overlaps the (060) reflection, impeding to characterize the smectite as trioctahedral or dioctahedral.

Smectites coexist with various primary and secondary minerals. Firstly, smectite is interstitial among olivine grains (Figs. 8c-e), forming randomly oriented irregular aggregates of about 300µm (Fig. 8e). Both olivine and smectite are crosscut by 10 to 100 µm wide veins of serpentine II (Fig. 8e). Secondly, smectite appears as rims around pyroxene (Figs. 8f-g). In this case, a core of enstatite is completely surrounded by smectite, which consists of tightly organized aggregates of fibrous-shaped crystals disposed perpendicularly to the pyroxene grain boundary. This assemblage is in turn crosscut by serpentine II (Fig. 8g). In addition, smectites are also found as partial replacements of enstatite with diopside exsolutions (Fig. 8h). Finally, smectite frequently showed strong alteration towards the borders (black in BSE images), in contact with serpentine II (Figs. 8i-k). These areas had high porosity and therefore EMP analyses were doubtful and had low oxide totals, but consist probably of quartz- or silica-rich aggregates with minor Fe oxyhydroxides. Similar features were observed surrounding smectites by Colin et al. (1985) and were described as amorphous.

### Silicified ferruginous saprolite

The silicified ferruginous saprolite corresponds to the uppermost 3 m of the core. It is brownish to reddish orange in color and is compact to friable (Fig. 5e). According to the powder X-ray diffractogram, it is composed of 75 wt.% quartz, 14 wt.% serpentine, 7 wt.% goethite, 4 wt.% hematite and 1 wt.% maghemite (Figs. 4, 5e). The study under optical and electron microscope reveals that serpentine has been replaced by Fe oxyhydroxides and silica (Fig. 9a).

Ni-Co-Mn-bearing phases (asbolanes) are more abundant in the silicified ferruginous saprolite than in the upper saprolite. These phases occur as vein infillings, in cracks developed by spheroidal weathering, and as coatings along joints (Fig. 9a-c). The Mn contents range from 11.46 to 69.87 wt.% MnO, and Ni and Co contents are remarkable, with up to 23.28 wt.% NiO and 6.51 wt.% CoO. On this basis, these Ni-Co-Mn-bearing phases are mostly Ni-rich asbolanes. Fe is highly variable, ranging from 0.13 to 24.23 wt.% $Fe_2O_3$. In general, these phases yield low Al (below 0.03 wt.% $Al_2O_3$).

## Mineral chemistry of the ore zone

### Ni-serpentine

In the saprolite zone, in which the whole rock MgO content slightly decreases and the NiO increases, Ni-poor serpentine from the ultramafic protolith (serpentine I) is progressively substituted by Ni-bearing serpentine (serpentine II). Ni and Fe contents in serpentine II are variable across the profile and at the microscopic scale (Fig. 7d).

Serpentine II contains 0.64-2.49 wt.% NiO (0.02-0.09 apfu Ni) and 2.63-7.85 wt.% $Fe_2O_3$ (0.04-0.28 apfu Fe), with an average structural formula of $(Mg_{2.60}Fe_{0.16}Ni_{0.06}Al_{0.04})Si_{2.02}O_5(OH)_4$ (32 analyses). In addition, serpentine II in contact with smectite grains yields the highest Ni (3.30-5.08 wt.% NiO, 0.14-0.20 apfu Ni) and Fe (4.53-13.47 wt.% $Fe_2O_3$, 0.17-0.53 apfu Fe), with an average structural formula of $(Mg_{2.46}Fe_{0.14}Ni_{0.18}Al_{0.01})Si_{2.04}O_5(OH)_4$ (6 analyses).

As observed above, the structural formulae of serpentine II from Loma Ortega present a marked deficiency in octahedral cations (Table 4), which was also observed by Golightly and Arancibia (1979) in a Ni-laterite profile from Indonesia, and this deficiency increases with increasing Ni and Fe substitution.

The relationships among the octahedral elements in the structure of Loma Ortega serpentines I and II is displayed in Fig. 10, and compared with serpentines I and II from the literature (Golightly and Arancibia 1979). As previously mentioned, serpentine II presents higher Ni contents than serpentine I. There is a well defined, negative correlation between Mg and Ni (Fig. 10a). On the contrary, Ni and Fe are positively correlated, and an increase of Ni and Fe may indicate a higher degree of weathering (Fig. 10b). However, according to the slope of the trend, Ni increases more rapidly than Fe, which is coherent with the observations by Golightly and Arancibia (1979) in serpentine II. Fe and Mg are also negatively correlated, although the trend is less defined than in Fig. 10a (Fig. 10c). When comparing Mg with Ni and Fe altogether, the negative correlation is more defined (Fig. 10d). This confirms that Mg is exchanged by Ni and Fe in the octahedral site of the serpentine.

### Garnierites

According to the XRD profile matching (Rietveld refinement), garnierite from Loma Ortega consists of a fine grained, intimate mixture of 95.2 wt.% kerolite-pimelite (talc with extra water in its structure, with a basal spacing of 10 Å), 3.7 wt.% lizardite and 1.1 wt.% quartz (Fig. 11a). The first basal reflection in talc-like garnierite is very broad and the remainder peaks are typical of a turbostratic structure with various degrees of asymmetry (Brindley and Hang 1973; Brindley et al. 1977; Brindley et al. 1979). Microprobe analyses give an average structural formula of

$(Ni_{1.95}Mg_{1.08}Fe_{0.01})(Si_{3.96}Al_{0.03})O_{10}(OH)_2\cdot nH_2O$ (average of 17 analyses). The Ni content ranges from 22.93 to 36.52 wt.% NiO (1.48-2.50 apfu Ni), with an average of 29.31 wt.% NiO (1.95 apfu Ni) (Table 5, Fig. 11b).

Given the X-ray diffractogram and the chemical composition, this garnierite can be classified as “talc-like” garnierite or pimelite. The textural features and the mineral composition match with the type IV garnierite described in Villanova-de-Benavent et al. (2014; 2016), and it is also comparable to the kerolite-pimelite described by Wells et al. (2009) and Cathelineau et al. (2016) in garnierite samples from New Caledonia.

### Ni-smectites

The composition of smectite from Loma Ortega is listed in Table 6 and represented in Figs. 12a-c. As observed in the ternary plots in Figs. 12a and 12c and in the binary diagram in Fig. 12b, its chemical composition is quite unique, when compared to other smectites from Ni-laterite deposits found in the literature (Bosio et al. 1975; Brindley et al. 1975; Nahon and Colin 1982; Nahon et al. 1982a; Colin et al. 1985; Decarreau et al. 1987; Pelletier 1996; Gaudin et al. 2004; 2005; Gleeson et al. 2004; Suárez et al. 2011).

The Al content is low (0.09-1.96 wt.% $Al_2O_3$, 0.01-0.20 apfu Al) and therefore the Al-for-Si substitution in the tetrahedral site is low (Fig. 12a). The Ni content is highly variable, but one of the highest reported in the literature, with 16.15-40.72 wt.% NiO (0.95-2.70 apfu Ni). The Fe content ranges from 1.11 to 6.00 wt.% $Fe_2O_3$ (0.08-0.38 apfu $Fe^{3+}$). The structural formulae reveal a trioctahedral smectite with the tetrahedral position fully occupied by Si and minor amounts of Al and $Fe^{3+}$ (Figs. 12a-b); with Ni and Mg as major octahedral cations (Figs. 12b-c). The average structural formula is $(Ca_{0.13}Na_{0.01})(Ni_{1.75}Mg_{1.30}Mn_{0.01})(Si_{3.76}Fe_{0.13}Al_{0.08}Cr_{0.03})O_{10}(OH)_2$ (average of 52 analyses).

## Discussion

### Geochemical and mineralogical evolution of the profile

In general whole rock analyses Fe and Mg show a typical geochemical evolution for a Ni-laterite profile in the Falcondo mining district: $Fe_2O_3$ increases from protolith (~8 wt.%) to saprolite (~10 wt.%) and reaches highest concentrations close to the surface (~18 wt.%), whereas MgO decreases from protolith (~37 wt.%) to saprolite (~33 wt.%) and shows a characteristic drop (down to ~2 wt.%) at higher levels of the profile. However, neither typically high $Fe_2O_3$ (>50 wt.%) values at the top nor a characteristic Mg discontinuity are observed. Interestingly, $SiO_2$ reveals a significant enrichment trend from protolith (~44 wt.%) towards the surface with highest concentrations of up to 68 wt.% at the top of the profile. This stands in contrast to previous observations from hydrous Mg silicate-type Ni-laterite profiles in the Falcondo mining district, where Si was observed to follow a very similar, decreasing trend as Mg from protolith to surface (e.g. Aiglsperger et al. 2016).

With respect to major elements the geochemical evolution of the profile is mainly explained by the breakdown of primary minerals (e.g. olivine and pyroxenes) which become unstable at surface temperatures and pressures in the presence of ground waters. Dissolved Mg is removed from the system, whereas Fe forms stable oxide(s) and dissolved Si reprecipitates as quartz in higher levels of the profile. This trend is well observed in the AF-M-S ternary diagram of Fig. 13 and explains constantly low UMIA values (<10) throughout the profile. However, the observed unusual quartz enrichment at Loma Ortega could be explained by a significantly higher water table and/or poor drainage which both lead to weathering of serpentine minerals with subsequent production of quartz and clay minerals (Golightly 1981). In addition, recent studies on mechanisms of mineral transformations associated with microbial dissolution of smectite have shown that silica of biogenic origin occurs (Dong et al. 2003). An allochtonous origin of $SiO_2$, as suggested by Gleeson et al. (2004) for the Cerro Matoso Ni-laterite deposit (Colombia), is not supported.

Regarding Ni, the geochemical evolution of the profile is closely related to the significant formation of Ni-enriched secondary phases such as serpentine II, garnierite and smectite starting at the transition zone between lower and upper saprolite (Fig. 2). This horizon marks the lower end of the ore zone which reaches concentrations of up to ~3wt.% Ni and ends with the sudden decrease of Mg and important increase of Si at a depth of ~2.5 m. In the upper saprolite (ore zone), Ni-poor, primary serpentine I is progressively replaced by Ni-bearing, secondary serpentine II (Fig. 7c). Apparently, serpentine II may result from a dissolution-precipitation process, accompanied by enrichment in Ni (as demonstrated by Villanova-de-Benavent et al. this volume), and/or from an exchange of Mg by Ni in the octahedral site, that produces a Ni enrichment, but essentially preserves the serpentine as a solid phase (Freyssinet et al. 2005). Further lateritization leads to the replacement of previous phases by fine-grained Fe-oxyhydroxides and cryptocrystalline quartz (Figs. 7a-d; e.g. Golightly 1981; Nahon et al. 1982), which are the main components of the silicified ferruginous saprolite at the top of the Loma Ortega profile (Figs. 2, 9a).

In addition, $Al_2O_3$ concentrations (~1 wt.% on average) show little variation throughout the profile. The absence of Al-rich phases and the low Al contents in garnierites, smectites and asbolanes is consistent with the Al-depleted composition of the parent rocks of the Loma Ortega deposit, mostly harzburgites with minor lherzolites and dunites (Proenza et al. 2007).

Finally, individual PGE concentrations are constantly low (<10 ppb) from protolith up to a depth of ~10 m where a slight enrichment trend is observed which reaches its highest value of 75 ppb total PGE at 5 m within the upper part of the ore zone. A residual nature of enrichment at this depth is supported by a coeval decrease of Mg. However, at highest levels of the profile Rh, Os, Ir and Ru drop down again to low concentrations (<10 ppb), whereas Pd and Pt reveal constant values of 4 ppb and 20 ppb, respectively. Pt enrichments at highest levels of Ni-laterites in the Falcondo mining district have been previously observed and are explained by dissolution – (biogenic) reprecipitation processes at low pH, high Eh conditions (Aiglsperger et al. 2015; 2016).

## The presence of high Ni smectites in a hydrous Mg silicate Ni-laterite deposit

Ni-smectites have been widely reported in various hydrous Mg silicate- and clay silicate-type Ni-laterite deposits worldwide, such as the Eight Dollar Mountain (SW Oregon, USA) (Hotz, 1964); Niquelândia and Barro Alto (Goiás State, Brazil) (Colin et al. 1985; Colin et al. 1990; Barros de Oliveira et al. 1992; Vieira Coelho et al. 2000); Murrin Murrin (Camuti and Gifford 1997; Gaudin et al. 2004; 2005) and Kalgoorlie (Elias et al. 1981) in Western Australia, and Greenvale in Queensland (Zeissink 1969), Australia; the Tiébaghi deposit (New Caledonia) (Pelletier 1996); Sipilou and Moyango (Western Ivory Coast) (Nahon and Colin 1982; Nahon et al. 1982a; 1982b); Cerro Matoso (Montelíbano, Colombia) (Gleeson et al. 2004) and San Felipe (Camagüey, Cuba) (Gallardo et al. 2011).

Most of the smectites reported in these localities are mixtures between dioctahedral and trioctahedral smectites, and show high Fe and remarkable Al contents, whereas those described in Loma Ortega are trioctahedral (Fig. 12a, b). However, unlike the trioctahedral smectites described in Tiébaghi, New Caledonia (Pelletier 1996), Cerro Matoso, Colombia (Gleeson et al. 2004) and Murrin Murrin, Australia (Gaudin et al. 2004; 2005), the smectites from Loma Ortega may reach high Ni contents, never reported before in the literature (Fig. 12c).

The compositions of olivine, enstatite and diopside from Loma Ortega (Table 3) are similar to those from Niquelândia (e.g. Colin et al. 1985) and Western Ivory Coast (Nahon et al. 1982a; 1982b). Therefore, the chemical differences between the smectites from Loma Ortega and the other localities might be explained by the relative amounts of primary minerals in the protolith instead of the composition of the primary minerals. In Niquelândia (Brazil), the protolith is mainly pyroxenite, leading to the formation of smectites with Al+Fe$^{3+}$ higher than Mg+Ni, and with low Ni contents, because pyroxene-dominated rocks (pyroxenites) contain more Al and Fe and less Ni than olivine-dominated rocks (dunites, harzburgites) (Colin et al. 1985; 1990).

Smectite is commonly believed to be formed after pyroxene (e.g. Colin et al. 1990), as an intermediate weathering stage previous to the formation of later Fe oxyhydroxides (e.g. Nahon and Colin 1982). According to Eggleton (1975), nontronite may grow topotactically from hedenbergite after the formation of a tetrahedral and an octahedral sheet from the shift of ½ [101] between adjacent pyroxene tetrahedral chains and octahedral cations. Actually, the **c** parameter of nontronite is approximately 1.5 times the **a** parameter of hedenbergite (Eggleton 1975), and this would facilitate the transformation of pyroxene to smectite.

On the other hand, Nahon et al. (1982a) interpreted that some smectites may form after olivine (see Figs. 1a, 2 in Nahon et al. 1982a). In the case of Loma Ortega, smectites were observed in contact not only with pyroxene (Fig. 12f-g), but also with olivine grains (Figs. 12c-e). In addition, given the denticulate contacts between smectite and olivine (Fig. 12e) and that all smectites contain very low Al contents, the olivine precursor cannot be discarded.

In Loma Ortega, smectites are usually crosscut by serpentine II (Figs. 12e, g, j), and the relationship between serpentine I and smectite could not be established. Nahon and Colin (1982) stated that there are no evidences of a direct replacement of primary lizardite (here serpentine I) by smectite because lizardite is more stable than olivine and pyroxene. Even so, Camuti and Gifford (1997) described that serpentine minerals were replaced by smectites in the Murrin Murrin Ni-laterite profile (Western Australia).

The clay silicate-type Ni-laterite profile at Murrin Murrin (Australia) is characterized by having two types of smectites: a) Mg-Ni trioctahedral smectites found in the saprolite zone, and b) Mg-Fe-Al dioctahedral smectites found in both the saprolite and smectite zones (Gaudin et al. 2005). These smectite compositions were included in Fig. 12 for the sake of comparison. However, in Loma Ortega smectites do not constitute a smectite layer, are constrained in the saprolite horizon and are exclusively trioctahedral. The evolution from Mg-Ni trioctahedral smectites to Fe-Al dioctahedral smectites has been widely reported in weathering profiles developed on ultramafic rocks (Gaudin et al. 2005 and references therein) and is consistent with thermodynamic models (Noack et al. 1993). Therefore, further maturation of the Loma Ortega profile might lead to the formation of a smectite zone with Fe-rich dioctahedral smectites, and the progressive transformation of the previous Ni-rich trioctahedral smectites into Fe oxyhydroxides (Colin et al. 1985).

Another particularity of Murrin Murrin is that there are no garnierites (Gaudin et al. 2005). After studying various weathering profiles worldwide, Golightly (1981) suggested that garnierites are absent when the protolith is totally serpentinized (like Murrin Murrin, Gaudin et al. 2005), whereas partially or non serpentinized rocks give rise to the formation of garnierites. Actually, the Ni-laterite deposits in New Caledonia, Brazil and Loma Ortega may contain both smectites and garnierites, because the protolith is not completely serpentinized. In addition, in São João do Piauí, in Brazil (Barros de Oliveira et al. 1992) smectites in the saprolite are found where the upper levels have strong silicification, and garnierite is related to profiles with strong silicification at all levels. The degree of silicification in the profile may depend on the climate of the area (silcrete is developed under tropical conditions, absent in arid climates). Therefore, the presence of garnierites and smectites altogether in the same laterite profile, and also the particularly high Ni contents of Loma Ortega smectites, are a consequence of the lateritization of a partially serpentinized olivine- (providing high Ni, in addition to percolating solutions from upper levels, and low Al contents) and pyroxene-bearing rocks.

Note that the formation of Ni-smectites by the replacement of primary minerals (olivine, pyroxene) differs from the formation of garnierites, which are neoformed minerals precipitated from Ni- and Si-saturated aqueous solutions into open spaces, often on a large scale (e.g. Villanova-de-Benavent et al. 2014).

## Implications on the mineralogical classification of Ni-laterite ore

In general, the Loma Ortega Ni-laterite profile broadly corresponds with the profiles observed in other deposits of the Falcondo district, as well as with other hydrous Mg silicate deposits worldwide (e.g. Aiglsperger et al. 2015; Villanova-de-Benavent et al. 2014). All of them are characterized by a thick serpentine-dominated saprolite horizon covered by a thin Fe-oxyhydroxide-dominated limonite horizon. The presence of Ni-smectite as a major ore mineral, typical of clay silicate-type Ni-laterites, is unusual at the Falcondo district. In the Loma Ortega laterite deposit, hydrous Mg silicate (Ni serpentine and garnierites) and clay (Ni-smectites) ores are confined to the same zone in the weathering profile, the upper saprolite horizon. Our data indicate that the Loma Ortega deposit has two types of ores, an hydrous silicate component and a clay silicate component. Therefore, the mineralogical classification of laterites according to the Ni ore is a simplification, as indicated by Golightly (2010). Berger et al. (2011) have concluded that Ni-laterite deposits of a “pure” type are rare and the deposit classification used depends on dominant nickel-bearing mineralogy in the laterite profile. According to the Ni-bearing mineral assemblage, Loma Ortega can be classified as a “hybrid hydrous Mg silicate-clay silicate” Ni-laterite deposit.

In other words, taking into account the characteristics of the smectite occurrences in the Loma Ortega, Tiébaghi, Niquelândia and Murrin Murrin laterite profiles, Loma Ortega can be described as a transition between a hydrous Mg silicate deposit and a clay silicate-type deposit. This is supported by the abundance and grade of Ni-bearing serpentine II in the saprolite zone, the presence of garnierite veinlets, the chemical composition of smectites and the absence of a smectite-rich layer (smectite zone).

## Conclusions

Trioctahedral Ni-smectites (Ni-Mg saponites) have been identified in slightly weathered, fractured hard saprolite from the Loma Ortega Ni-laterite deposit in the western part of the Loma Caribe serpentinized peridotite massif. This is the first time Ni-rich saponites (containing up to 33 wt.% NiO) have been described in Ni-laterites formed from ophiolitic harzburgites.

According to the main Ni-bearing minerals, the Loma Ortega profile can be classified as a “hybrid hydrous Mg silicate – clay silicate” type Ni-laterite, in which most of the Ni is present in Ni-bearing, secondary serpentines II, smectites and garnierites. Serpentine II is formed by reaction of meteoric waters with Ni-poor, primary serpentine I. In contrast, smectites are formed by the interaction of the primary pyroxenes or olivines from harzburgites with Ni-enriched, meteoric solutions, during the first stage of the lateritization process, before alteration and final oxidation of the profile. The composition of the smectite is determined by the mineralogy of the protolith and by the composition of percolating solutions. In the case of Loma Ortega, an Al-depleted, olivine-rich protolith leaded to the formation of Ni-Mg saponites. However, it is worth noting that unlike garnierites, which precipitate from Ni-saturated solutions in open spaces, smectites occupy interstitial positions surrounded by primary minerals (olivine and pyroxene), and are previous to the formation of Ni-enriched serpentine II.

## Acknowledgements

This research has been financially supported by FEDER Funds, the Spanish projects CGL2009-10924 and CGL2012-36263. The authors are grateful to the Falcondo Glencore Xstrata Nickel mine staff for their hospitality and generosity during field work and sampling.

## References

Aiglsperger T, Proenza JA, Zaccarini F, Lewis JF, Garuti G, Labrador M, Longo F (2015) Platinum group minerals (PGM) in the Falcondo Ni-laterite deposit, Loma Caribe peridotite (Dominican Republic). Miner Deposita 50:105-123

Aiglsperger T, Proenza JA, Lewis JF, Labrador M, Svojtka M, Rojas-Purón A, Longo F, Ďurišová J (2016) Critical metals (REE, Sc, PGE) in Ni-laterites from Cuba and the Dominican Republic. Ore Geol Rev 73: 127-147

Barros de Oliveira SM, Trescases JJ, Melfi AJ (1992) Lateritic nickel deposits of Brazil. Miner Deposita 27: 137-146

Berger VI, Singer DA, Bliss JD, Moring BC (2011) Ni-Co laterite deposits of the world; database and grade and tonnage models: U.S. Geological Survey Open-File Report 2011-1058 [http://pubs.usgs.gov/of/2011/1058/]

Bosio NJ, Hurst VJ, Smith RL (1975) Nickeliferous nontronite, a 15 Å garnierite, at Niquelândia, Goiás, Brazil. Clay Clay Miner 23: 400-403

Bowin CO (1966) Geology of the central Dominican Republic (a case history of part of an island arc). In: Hess H (Ed.) Caribbean Geological Studies. Mem Geol Soc Am 98: 11-84

Brand NW, Butt CRM, Elias M (1998) Nickel laterites: classification and features. AGSO J Australian Geol Geoph 17: 81-88

Brindley GW, de Souza JV (1975) Nickel containing montmorillonites and chlorites from Brazil, with remarks on schuchardtite. Mineral Mag 40: 141-152

Brindley GW, Bish D, Wan HM (1977) The nature of kerolite, its relation to talc and stevensite. Mineral Mag 41: 443-452

Brindley GW, Bish DL, Wan HM (1979) Compositions, structures, and properties of nickel-containing minerals in the kerolite-pimelite series. Am Mineral 64: 615-625

Brindley GW, Hang PT (1973) The nature of garnierite: I. Structure, chemical compositions and color characteristics. Clay Clay Miner 21: 27-40

Bruker (2007) Bruker AXS Inc., Madison, Wisconsin, USA

Butt CRM, Cluzel D (2013) Nickel laterite ore deposits: weathered serpentinites. Elements 9: 123-128

Camuti KS, Gifford MG (1997) Mineralogy of the Murrin Murrin nickel laterite deposit, western Australia. In: Papunen H (Ed.), Mineral Deposits: Research and Exploration - Where Do They Meet? Abstracts of the 4th Meeting of the SGA, 407-410.

Cathelineau M, Quesnel B, Gautier P, Boulvais P, Couteau C, Drouillet M (2016) Nickel dispersion and enrichment at the bottom of the regolith: formation of pimelite target-like ores in rock block joints (Koniambo Ni deposit, New Caledonia) Miner Deposita 51: 271-282

Chan TK, Finch IJ (2001) Determination of platinum-group elements and gold by inductively coupled plasma mass spectrometry. Australian Platinum Conference, Perth, Western Australia: 1-9

Colin F, Nahon D, Trescases JJ, Melfi AJ (1990) Lateritic Weathering of Pyroxenites at Niquelandia, Goias, Brazil: The Supergene Behaviour of Nickel. Econ Geol 85: 1010-1023

Colin F, Noack Y, Trescases JJ, Nahon D (1985) L’alteration latéritique débutante des pyroxenites de Jacuba, Niquelândia, Brésil. Clay Miner 20: 93-113

Dalvi AD, Gordon Bacon W, Osborne RC (2004) The past and the future of nickel laterites. PDAC Int. Convention, Toronto, Canada, p. 27

Decarreau A, Colin F, Herbillon A, Manceau A, Nahon D, Paquet H, Trauth-Badaud D, Trescases JJ (1987) Domain segregation in Ni-Fe-Mg-smectites. Clay Clay Miner 35: 1-10

Dong HL, Kostka JE, Kim J (2003) Microscopic evidence for microbial dissolution of smectite. Clay Clay Miner 51: 502-512

Draper G, Gutiérrez G, Lewis JF (1996) Thrust emplacement of the Hispaniola peridotite belt: Orogenic expression of the mid-Cretaceous Caribbean arc polarity reversal? Geology 24: 1143-1146

Eggleton RA (1975) Nontronite topotaxial after hedenbergite. Am Mineral 6: 1063-1068

Elias M, Donaldson MJ, Giorgetta N (1981) Geology, Mineralogy, and Chemistry of Lateritic Nickel-Cobalt Deposits near Kalgoorlie, Western Australia. Econ Geol 76: 1775-1783

Elias M (2002) Nickel laterite deposits—Geological overview, resources and exploration. In: Cooke D, Pongratz J (Eds.), Giant ore deposits—Characteristics, genesis, and exploration. CODES Special Publication 4, University of Tasmania, Hobart, p. 205-220.

Escuder-Viruete J, Pérez-Estaún A, Contreras F, Joubert M, Weis D, Ullrich TD, Spadea P (2007) Plume mantle source heterogeneity through time: insights from the Duarte Complex, Hispaniola, northeastern Caribbean. J Geophys Res 112: B04203

Escuder-Viruete J, Joubert M, Urien P, Friedman R, Weis D, Ullrich T, Pérez-Estaún A (2008) Caribbean island-arc rifting and back-arc basin development in the Late Cretaceous: geochemical, isotopic and geochronological evidence from Central Hispaniola. Lithos 104, 378-404

Escuder-Viruete J, Pérez-Estaún A, Weis D, Friedman R (2010) Geochemical characteristics of the Río Verde Complex, Central Hispaniola: implications for the paleotectonic reconstruction of the Lower Cretaceous Caribbean island-arc. Lithos 114, 168-185

Freyssinet Ph, Butt CRM, Morris RC (2005) Ore-forming processes related to lateritic weathering: Econ Geol 100th Anniv Vol:681-722

Gallardo T, Tauler E, García-Romero E, Proenza JA, Suárez-Barrios M, Chang A (2011) Caracterización Mineralógica de las Esmectitas Niquelíferas del yacimiento de San Felipe (Camagüey, Cuba). Macla 15: 89-90.

Gaudin A, Grauby O, Noack Y, Decarreau A, Petit S (2004) Accurate crystal chemistry of ferric smectites from the lateritic nickel ore of Murrin Murrin (Western Australia). I XRD and multi-scale chemical approaches. Clay Miner 39: 301-315

Gaudin A, Decarreau A, Noack Y, Grauby O (2005) Clay mineralogy of the nickel laterite ore developed from serpentinised peridotites at Murrin Murrin, Western Australia. Australian J Earth Sci 52: 231-241

Gleeson SA, Butt CR, Elias M (2003) Nickel laterites: A review: SEG Newsletter 54:11-18

Gleeson SA, Herrington RJ, Durango J, Velásquez CA, Koll G (2004) The mineralogy and geochemistry of the Cerro Matoso S.A. Ni-laterite deposit, Montelíbano, Colombia. Econ Geol 99: 1197-1213

Golightly JP (1981) Nickeliferous laterite deposits. Econ Geol 75th Anniv Vol:710-735

Golightly JP (2010) Progress in understading the evolution of nickel laterites. Econ Geol Spec Pub 15:451-485

Golightly JP, Arancibia ON (1979) The Chemical composition and infrared spectrum of nickel- and iron-substituted serpentine form a nickeliferous laterite profile, Soroako, Indonesia. Can Mineral 17: 719-728

Haldemann E, Buchan R, Blowes J, Chandler T (1979) Geology of lateritic nickel deposits, Dominican Republic. International Laterite Symposium 4: 57-84

Hotz P (1964) Nickeliferous Laterites in Southwestern Oregon and Northwestern California. Econ Geol 59: 355-396

Kesler SE, Campbell IH, Allen CM (2005) Age of the Los ranchos formation, Dominican Republic: timing and tectonic setting of primitive island arc volcanismin the Caribbean region. Geol. Soc. Am. Bull. 117, 987-995

Kuck PH (2013) Nickel. USGS Mineral Commodity Summaries 108-109

Lewis JF, Astacio VA, Espaillat J, Jiménez J (2000) The occurrence of volcanogenic massive sulfide deposits in the Maimón Formation, Dominican Republic: the Cerro de Maimón, Loma Pesada and Loma Barbuito deposits. In: Sherlock, R., Barsch, R., Logan, A. (Eds.), VMS Deposits of Latin America. Geol. Soc. Can. Spec. Publ. 2, p. 213-239

Lewis JF, Draper G (1990) Geological and tectonic evolution of the northern Caribbean margin. In: Dengo G, Case JE (Eds.). The Geology of North America, Volume H: The Caribbean region. Geological Society of America, Colorado, p. 77-140.

Lewis JF, Draper G, Proenza JA, Espaillat J, Jimenez J (2006) Ophiolite-related ultramafic rocks (serpentinites) in the Caribbean Region: A review of their occurrence, composition origin, emplacement and Ni-laterite soils formation. Geol Acta 4: 237-263

Lithgow E (1993) Nickel laterites of central Dominican Republic Part I. Mineralogy and ore dressing. In: Reddy, R.G., Weizenbach, R.N. (Eds.), The Paul E. Queneau Int.

Symposium, Extractive Metallurgy of Copper, Nickel and cobalt, Volume I: Fundamental aspects. The Minerals, Metals and Materials Society, Portland, 403-42

Marchesi C, Garrido CJ, Proenza JA, Hidas K, Butjosa L, Lewis JF (2016) Geochemical record of subduction initiation in the sub-arc mantle: Insights from the Loma Caribe peridotite (Dominican Republic). Lithos 252–253: 1-15

Nahon DB, Colin F (1982) Chemical weathering of orthopyroxenes under lateritic conditions. Am J Sci 282: 1232-1243

Nahon DB, Colin F, Tardy Y (1982a) Formation and distribution of Mg, Fe, Mn-smectites in the first stages of the lateritic weathering of forsterite and tephroite. Clay Miner 17: 339-348

Nahon DB, Paquet H, Delvigne J (1982b) Lateritic Weathering of Ultramafic Rocks and the Concentration of Nickel in the Western Ivory Coast. Econ Geol 77: 1159-1175

Naldrett AJ, Duke JM (1980) Platinum metals in magmatic sulfide ores. Science 208: 1417-1424

Nelson CE, Proenza JA, Lewis JF, López-Kramer J (2011) The metallogenic evolution of the Greater Antilles. Geol Acta 9: 229-264

Noack Y, Colin F, Nahon D, Delvigne J, Michaux L (1993) Secondary-mineral formation during natural weathering of pyroxene: review and thermodynamic approach. Am J Sci 293: 111-134

Pelletier B (1996) Serpentines in nickel silicate ore from New Caledonia. Australasian Institute of Mining and Metallurgy Publication Series - Nickel conference “Mineral to market”, Kalgoorlie, Western Australia 6/96: 197-205

Proenza JA, Tauler E, Melgarejo JC, Galí S, Labrador M, Marrero N, Pérez-Melo N, Rojas-Purón AL, Blanco-Moreno JA (2007) Mineralogy of oxide and hydrous silicate Ni-laterite profiles in Moa Bay area, northeast Cuba. In: Andrew et al. (eds.), Digging Deeper, Irish Association for Economic Geology, Dublin, Ireland. 2: 1389-1392

Redwood S (2014) Gold surge mining is booming in the Dominican Republic as investors follow the gold rush. Min J 24: 23-27

Suárez S, Nieto F, Velasco F, Martín FJ (2011) Serpentine and chlorite as effective Ni-Cu sinks during weathering of the Aguablanca sulphide deposit (SW Spain). TEM evidence for metal-retention mechanisms in sheet silicates. Eur J Miner 23: 179-196

Tauler E, Proenza J, Galí S, Lewis J, Labrador M, García-Romero E (2009) Ni-sepiolite-falcondoite in garnierite mineralisation from the Falcondo Ni-laterite deposit, Dominican Republic. Clay Miner 44: 435-454

Torró L, Proenza JA, Farré de Pablo J, Colomer JM, García-Casco A, Melgarejo JC, Alfonso P, Gubern A, Gallardo E, Cazañas X, Chávez C, del Carpio R, León P, Espaillat J, Lewis JF (2016) Mineralogy, geochemistry and sulfur isotope characterization of Cerro de Maimón (Dominican Republic), San Fernando and Antonio (Cuba) Lower Cretaceous VMS deposits: formation during subduction initiation of the Proto-Caribbean lithosphere within a fore-arc. Ore Geol Rev 72: 794-817

Trescases JJ (1975) L'évolution géochimique supergène des roches ultrabasiques en zone tropicale et la formation des gisements nickélifères de Nouvelle-Calédonie. Mémoires ORSTOM 78, p. 288

Vieira Coelho AC, Poncelet G, Ladrière J (2000) Nickel, iron-containing clay minerals from Niquelândia deposit, Brazil 1. Characterization. Appl Clay Sci 17: 163-181

Villanova-de-Benavent C, Proenza JA, Galí S, García-Casco A, Tauler E, Lewis JF, Longo F (2014) Garnierites and garnierites: Textures, mineralogy and geochemistry of garnierites in the Falcondo Ni-laterite deposit, Dominican Republic. Ore Geol Rev 58: 91-109

Villanova-de-Benavent C, Nieto F, Viti C, Proenza JA, Galí S, Roqué-Rosell J (2016) Ni-phyllosilicates (garnierites) from the Falcondo Ni-laterite deposit (Dominican Republic): mineralogy, nanotextures and formation mechanisms by HRTEM and AEM. Am Mineral. DOI: http://dx.doi.org/10.2138/am-2015-5518

Villanova-de-Benavent C, Domènech C, Tauler E, Galí S, Tassara S, Proenza JA (this volume) Fe-Ni-bearing Serpentines from the Saprolite Horizon of Caribbean Ni-Laterite Deposits: New Insights from Thermodynamic Calculations. Miner Deposita

Wells MA, Ramanaidou ER, Verrall M, Tessarolo C (2009) Mineralogy and crystal chemistry of "garnierites" in the Goro lateritic nickel deposit, New Caledonia. Eur J Miner 21: 467-483

Zeissink HE (1969) The Mineralogy and Chemistry of a Nickeliferous Laterite Profile (Greenvale, Queensland, Australia). Mineral Deposita 4: 132-152

## Figures and tables

**Figure 1.** A) Simplified geological map of the central section of the Loma Caribe peridotite showing the location of the Loma Ortega ore deposit (modified from Bowin 1966; Escuder-Viruete et al. 2007). B) Orthophotograph showing the Falcondo mining area with the Loma Ortega and other ore deposits; the location of investigated drill core O954-0307 is highlighted.

**Figure 2.** Ni laterite profile from drill core O954-0307 (Loma Ortega) showing location of samples with major (Si, Mg, Fe and Al), Ni and PGE contents. Data from 35.9 to 41.3 m is not presented to avoid redundancy.

**Figure 3.** Chondrite normalized PGE patterns of samples from drill core O954-0307 (Loma Ortega) with indicated fields of limonite, saprolite and parent rock from samples from the Loma Caribe and Loma Peguera ore deposits (Falcondo mining area) (Aiglsperger et al. 2015). Note the positive Pt anomaly at 0.5 m. Normalization values from Naldrett and Duke (1980).

**Figure 4.** Proportion of minerals in 22 samples according to the depth, obtained by Rietveld refinement of powder X-ray diffractograms by using the TOPAS v4.2 software.

**Figure 5.** Hand specimen images and corresponding powder X-ray diffractograms of selected, representative samples from the different zones identified in the core from Loma Ortega: a) serpentinized peridotite (sample LO-55, 41.3-41.4 m depth); b) lower saprolite (sample LO-23.5, 23.5 m depth); c) upper saprolite with smectite (sample LO-53A, 16.7-17 m depth); d) upper saprolite (sample LO-52A, 8-8.3 m depth); e) silicified ferruginous saprolite (sample LO-51, 0.3-0.45 m depth). Legend: forsterite (Fo), lizardite (Lz), magnetite (Mt), Cr-spinel (Chr), diopside (Di), enstatite (En), smectite (Sm), maghemite (Mgh), goethite (Gth), hematite (Hem), quartz (Qz). Ni-bearing minerals are in bold.

**Figure 6.** Optical (a, b) and backscattered electron images (c, d, e, f) of the characteristic textures of primary minerals (pre-weathering) in the Loma Ortega Ni-laterite profile. General features of a) serpentine (Srp) in foliated, serpentinized peridotite (sample LO-55, 41.3-41.4 m) and b) olivine (Ol) and pyroxene (Px) in slightly weathered harzburgite from the lower saprolite zone (sample LO-18.5, 18.5 m) under crossed polars. c-e) Textural relationships among olivine (Ol), diopside (Di) and enstatite (En) at the lower saprolite zone (c: LO-17.6, 17.6 m; d-e: LO-53B, 18 m). f) Cr-spinel (Chr) with an alteration rim of Fe oxides (FeOx) from the upper saprolite zone (sample LO-53, 10.5 m).

**Figure 7.** Optical (a, f: parallel light; b: crossed polars), backscattered electron images (c, d, g) and hand specimen image (e) of secondary minerals in the upper saprolite zone: a-c) yellowish serpentine II (Srp) veins surrounding brownish quartz (Qz) and goethite (Gth) aggregates (LO-53A2, 16.7 m); d) asbolane (A) coexisting with quartz and goethite aggregates (LO-52A, 8-8.3 m) surrounded by serpentine II (LO-52A, 8-8.3 m); e-g) pale green garnierite (G) included in a greenish white, translucent quartz matrix (Qz) (LO-53A, 16.7 m).

**Figure 8.** Mineralogy and textures of Ni-smectites from the Loma Ortega core: a) X-ray microdiffractogram with the corresponding X-ray image and the reflected light, optical micrograph depicting the analyzed area with a white rectangle (approximately 500 µm long); b) untreated, glycolated and heated, oriented mount X-ray powder diffractograms; optical (c, d, f, i) and backscattered electron (e, g, h, j, k) micrographs of Ni-bearing smectites from the Loma Ortega core: c-e) parallel light (c), crossed polars (d) and BSE (e) images of smectite (Sm) coexisting with olivine (Ol), crosscut by serpentine II (Srp); f-g) parallel light (f), and BSE (g) images of smectite (Sm) coexisting with enstatite (Px), crosscut by serpentine II (Srp); h) BSE image of diopside (Di) exsolution in enstatite (En), both being replaced by smectite (Sm); i-k) parallel light (i) and BSE images (j, k) of smectite (Sm) crosscut by serpentine II (Srp) veinlets (samples LO-53A and LO-53A2, 16.7 m).

**Figure 9.** Optical, crossed polars (a) and backscattered electron images (b-c) of secondary minerals in the silicified ferruginous saprolite of the Loma Ortega core (sample LO-51, 0.3-0.45 m depth): a) goethite (Gth) matrix with quartz (Qz) veinlet surrounding a Cr-spinel relict (Chr); b-c) asbolane (A) as veinlet infillings.

**Figure 10.** Comparison between the major octahedral elements (Ni-Mg (a); Ni-Fe (b); Fe-Mg (c); Ni+Fe-Mg (d)) in lizardite I and II in the studied core from Loma Ortega, compared with primary and secondary serpentines from Indonesia of Golightly and Arancibia (1979).

**Figure 11.** Powder XRD diffractogram (a) and (Mg+Fe)-Si-Ni ternary plot (b) depicting the mineralogy and chemical composition of garnierites from the Loma Ortega ore deposit. It includes data from other ore deposits in the Falcondo mining area for comparison (modified from Villanova-de-Benavent et al. 2014).

**Figure 12.** Mineral chemistry of Ni-smectites from the Loma Ortega core (sample LO-53A2, 17 m depth): a) $Fe^{3+}$-Al-(Mg+Ni) ternary plot (based on Colin et al. 1985); b) $Fe^{3+}$ versus Mg+Ni binary diagram representing the octahedral cations in smectites (modified from Colin et al. 1985); and c) Ni-Mg-$Fe^{3+}$ ternary plot, comparing the composition of Ni-smectites from Loma Ortega to those found in Murrin Murrin, Australia (Gaudin et al. 2004; 2005); Niquelândia, Brazil (Bosio et al. 1975; Brindley et al. 1975; Colin et al. 1985; Decarreau et al. 1987); Cerro Matoso, Colombia (Gleeson et al. 2004); Western Ivory Coast (Nahon and Colin 1982; Nahon et al. 1982a); Tiébaghi, New Caledonia (Pelletier 1996) and Aguablanca, Spain (Suárez et al. 2011).

**Figure 13.** Molar ternary plot in the Al-Fe-Mg-Si space showing the weathering trend of ultramafic rocks and their relationships with the ultramafic index of alteration (UMIA) with data from the literature and studied samples (modified from Aiglsperger et al. 2016).

**Table 1.** Concentrations of relevant major elements (in wt.%) as well as Ni (in %) in samples from drill core O954-0307. UMIA (ultramafic index of alteration) after Aiglsperger et al. (2016). Data from 35.9 to 41.3 m is not presented to avoid redundancy

**Table 2. .** Concentrations of PGE (in ppb) in samples from drill core O954-0307. Data from 35.9 to 41.3 m is not presented to avoid redundancy

**Table 3.** Representative EMP analyses (in weight percent) and calculated structural formulae (in atoms per formula unit) of olivine, enstatite, diopside and Cr-spinel.

**Table 4.** Representative EMP analyses (in weight percent) and calculated structural formulae (in atoms per formula unit) of serpentine I and serpentine II.

**Table 5.** Representative EMP analyses (in weight percent) and calculated structural formulae (in atoms per formula unit) of garnierites.

**Table 6.** Representative EMP analyses (in weight percent) and calculated structural formulae (in atoms per formula unit) of Ni-smectites.

Figure 1

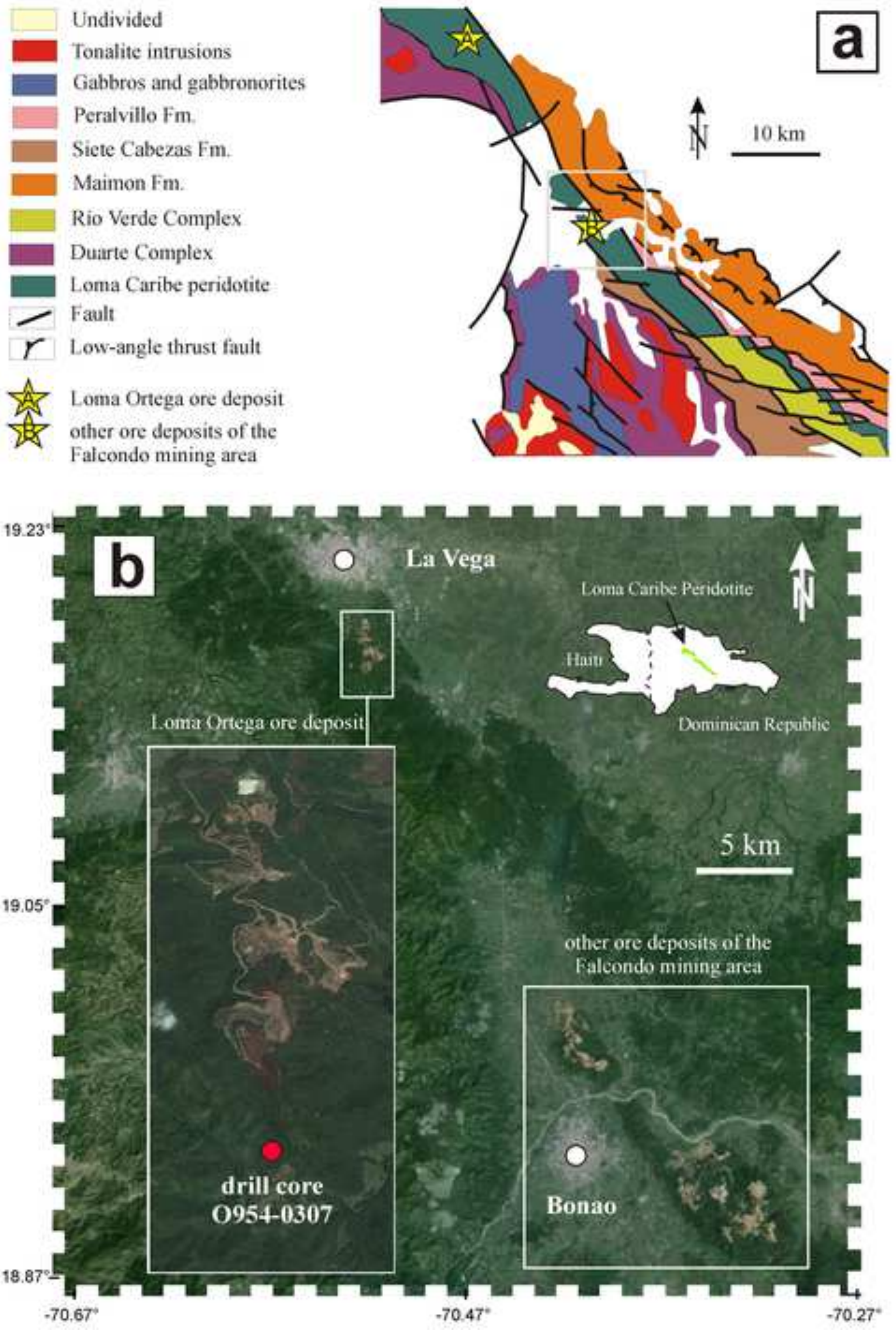
Undivided
Tonalite intrusions
Gabbros and gabbronorites
Peralvillo Fm.
Siete Cabezas Fm.
Maimon Fm.
Rio Verde Complex
Duarte Complex
Loma Caribe peridotite
Fault
Low-angle thrust fault
A Loma Ortega ore deposit
B other ore deposits of the Falcondo mining area
a
A
B
N
10 km
b
19.23°
19.05°
18.87°
-70.67°
-70.47°
-70.27°
La Vega
Loma Caribe Peridotite
N
Haiti
Dominican Republic
Loma Ortega ore deposit
5 km
other ore deposits of the Falcondo mining area
drill core O954-0307
Bonao

Figure 2

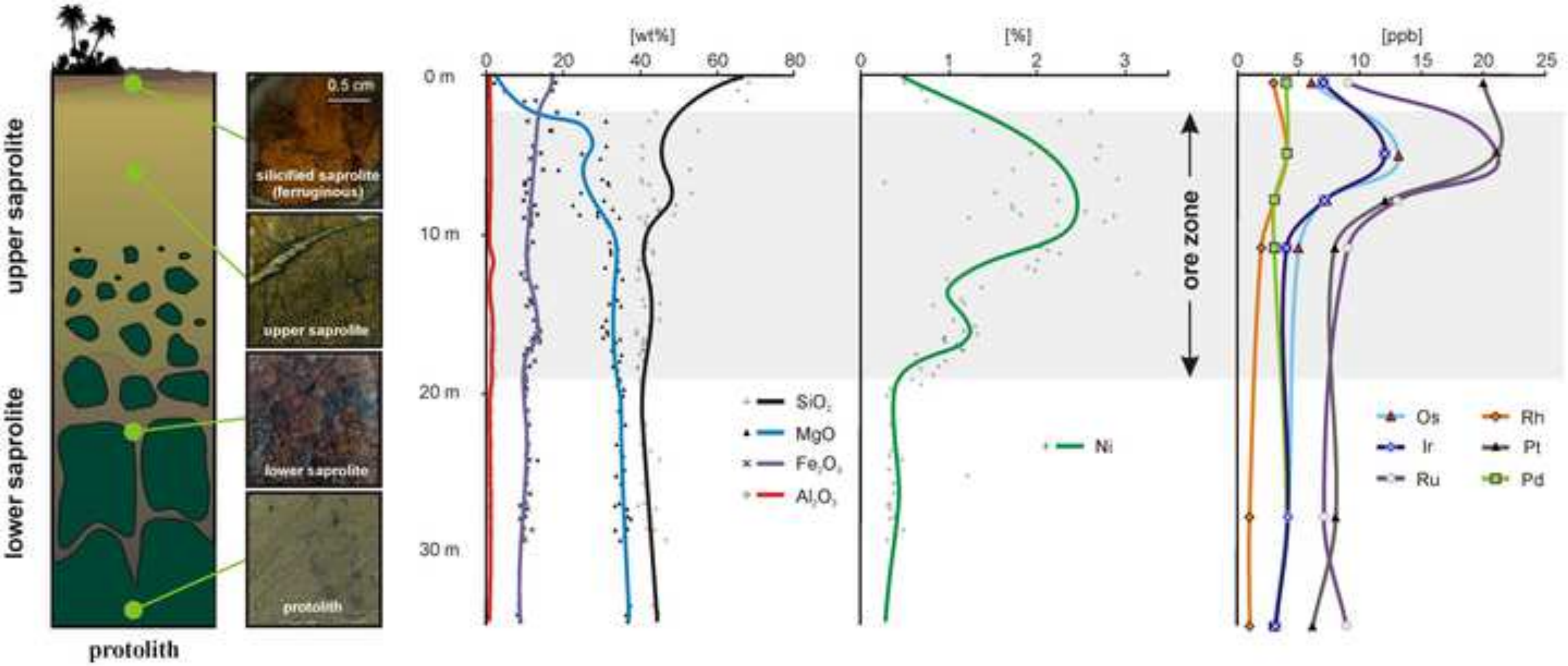
upper saprolite
lower saprolite
protolith
0.5 cm
silicified saprolite (ferruginous)
upper saprolite
lower saprolite
protolith
[wt%]
0
20
40
60
80
0 m
10 m
20 m
30 m
$SiO_2$
MgO
$Fe_2O_3$
$Al_2O_3$
[%]
0
1
2
3
Ni
ore zone
[ppb]
0
5
10
15
20
25
Os
Rh
Ir
Pt
Ru
Pd

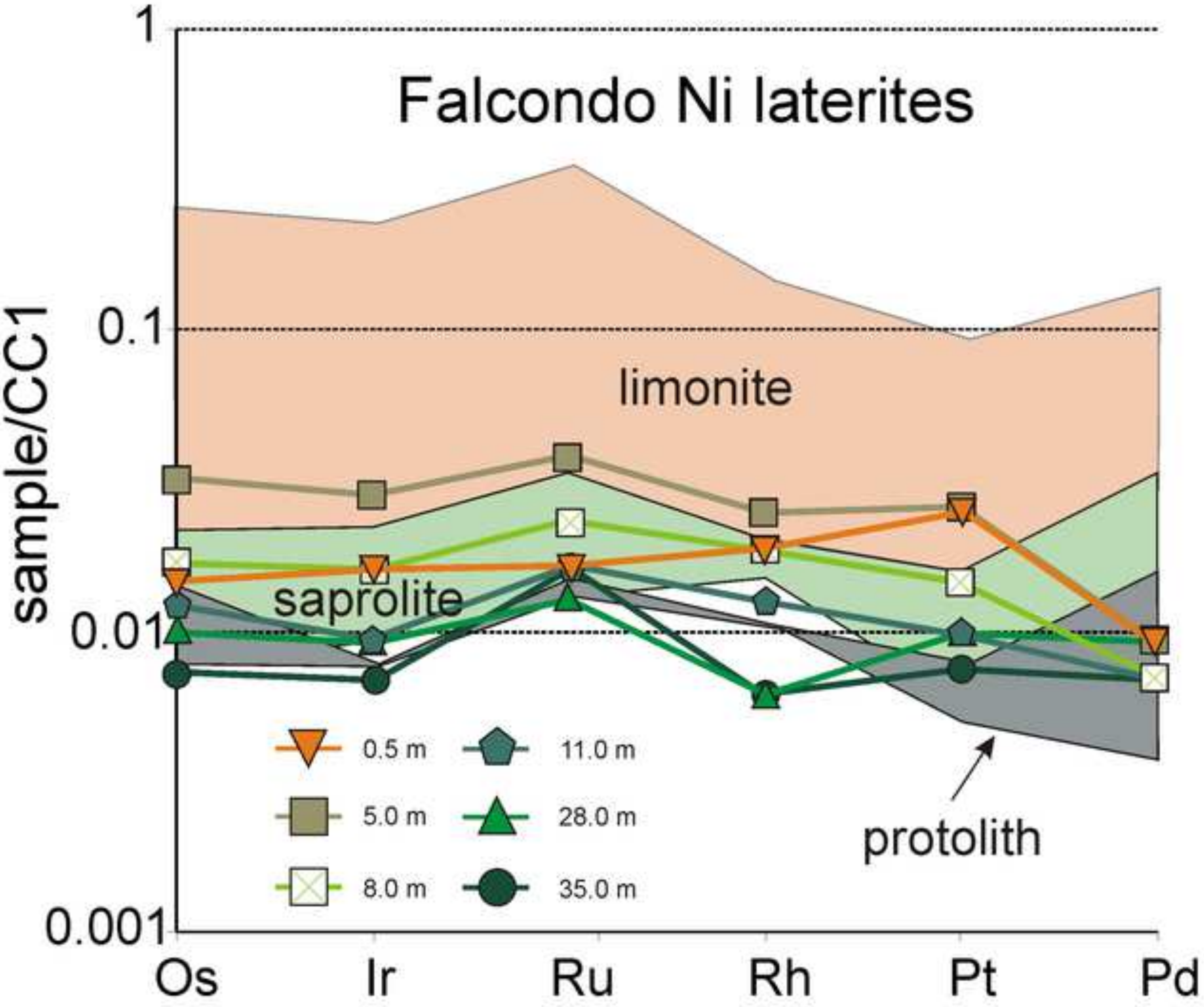
Falcondo Ni laterites
sample/CC1
1
0.1
0.01
0.001
limonite
saprolite
protolith
0.5 m
5.0 m
8.0 m
11.0 m
28.0 m
35.0 m
Os
Ir
Ru
Rh
Pt
Pd

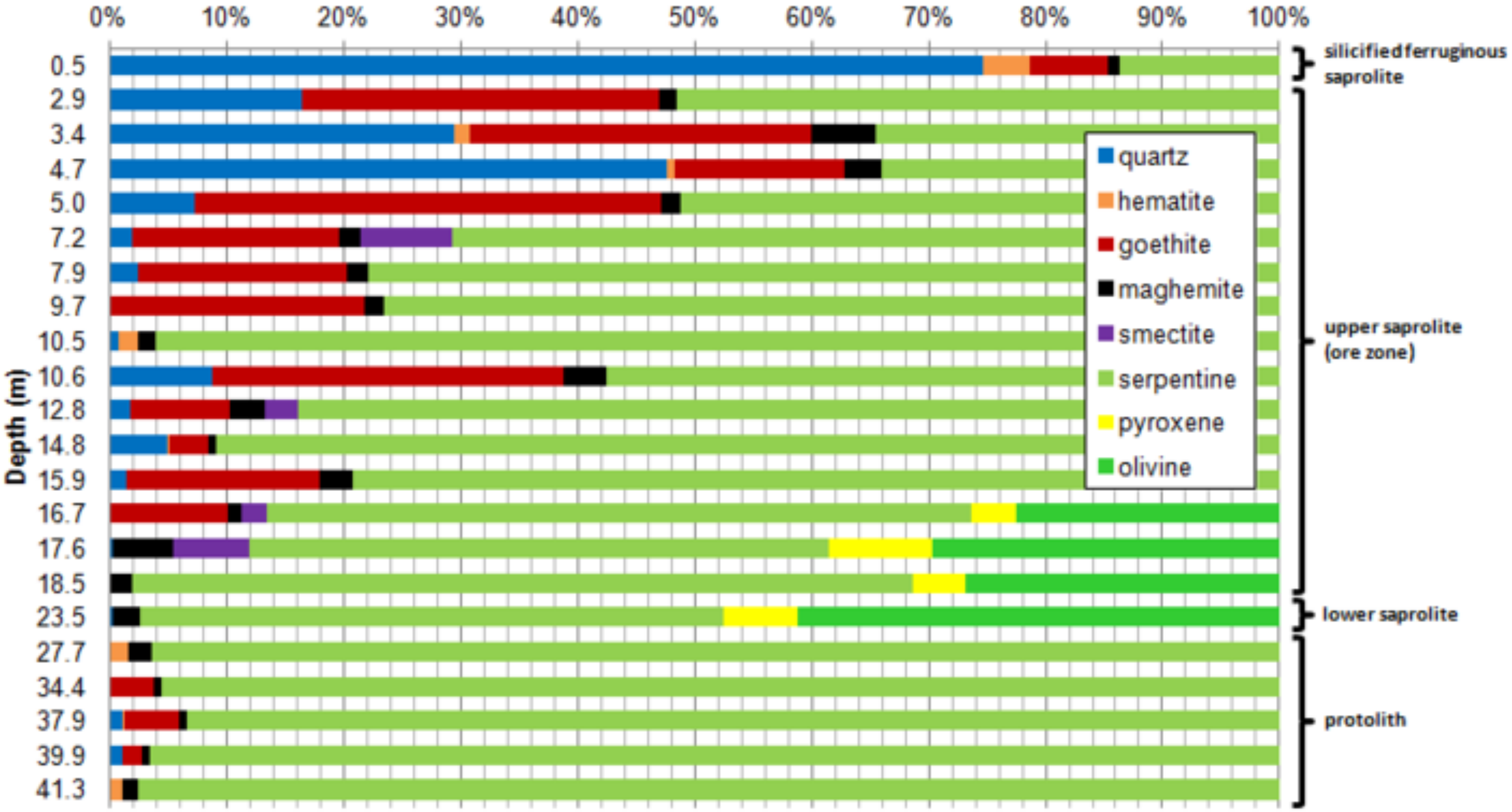
0%
10%
20%
30%
40%
50%
60%
70%
80%
90%
100%
Depth (m)
0.5
2.9
3.4
4.7
5.0
7.2
7.9
9.7
10.5
10.6
12.8
14.8
15.9
16.7
17.6
18.5
23.5
27.7
34.4
37.9
39.9
41.3
quartz
hematite
goethite
maghemite
smectite
serpentine
pyroxene
olivine
silicified ferruginous saprolite
upper saprolite (ore zone)
lower saprolite
protolith

Figure 5

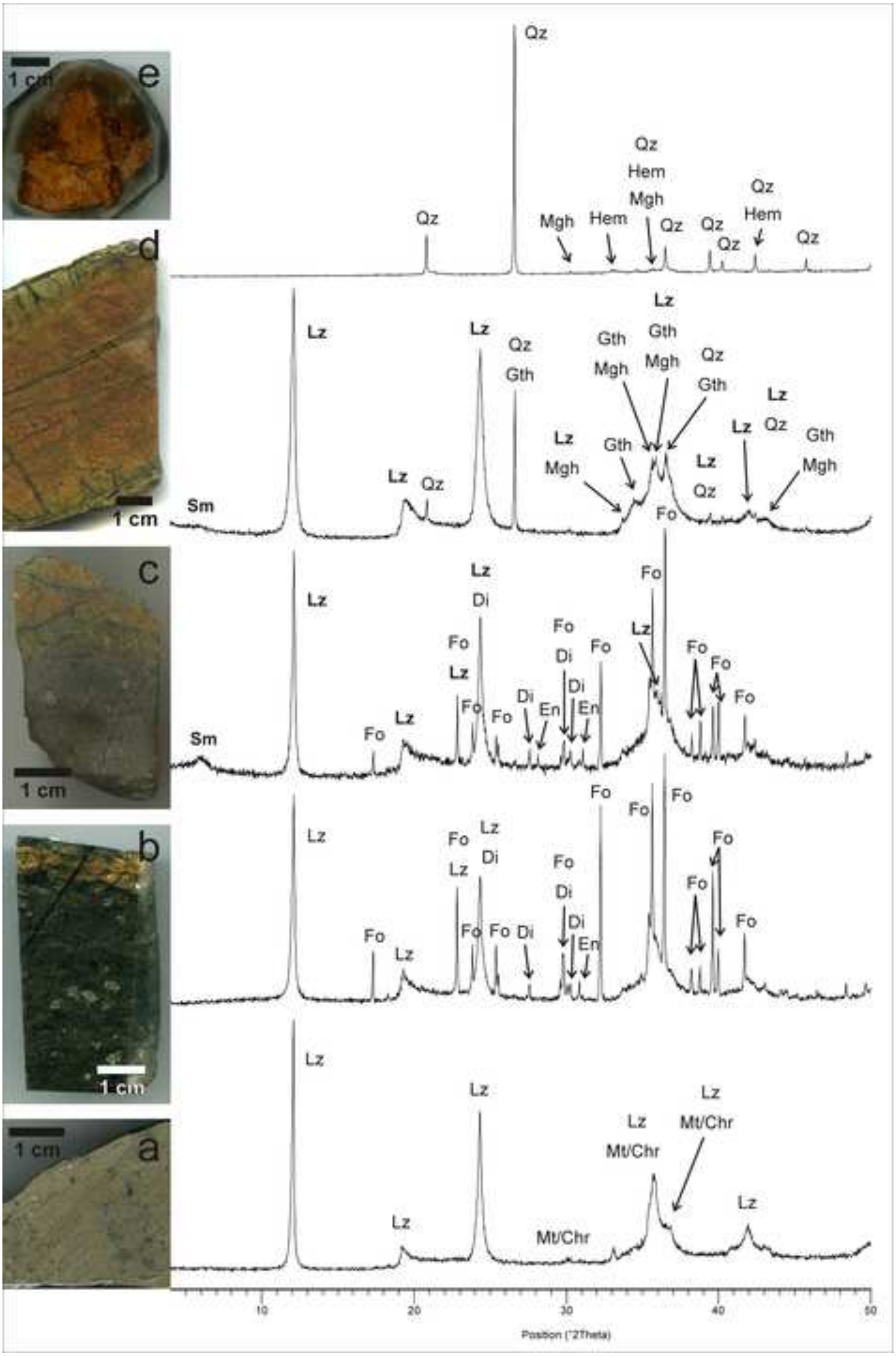
e
1 cm
Qz
Qz
Mgh
Hem
Qz
Hem
Mgh
Qz
Qz
Qz
Qz
Hem
Qz
d
1 cm
Sm
Lz
Lz
Qz
Lz
Qz
Gth
Lz
Mgh
Gth
Mgh
Gth
Lz
Gth
Mgh
Qz
Gth
Lz
Lz
Qz
Lz
Qz
Gth
Mgh
Fo
c
1 cm
Sm
Lz
Fo
Lz
Fo
Lz
Lz
Di
Fo
Fo
Di
Fo
Di
En
Fo
Di
Di
En
Fo
Lz
Fo
Fo
Fo
Fo
b
1 cm
Lz
Fo
Lz
Fo
Lz
Lz
Di
Fo
Fo
Di
Fo
Di
Di
En
Fo
Fo
Fo
Fo
Fo
Fo
a
1 cm
Lz
Lz
Lz
Mt/Chr
Lz
Mt/Chr
Lz
Mt/Chr
Lz
10
20
30
40
50
Position (°2Theta)

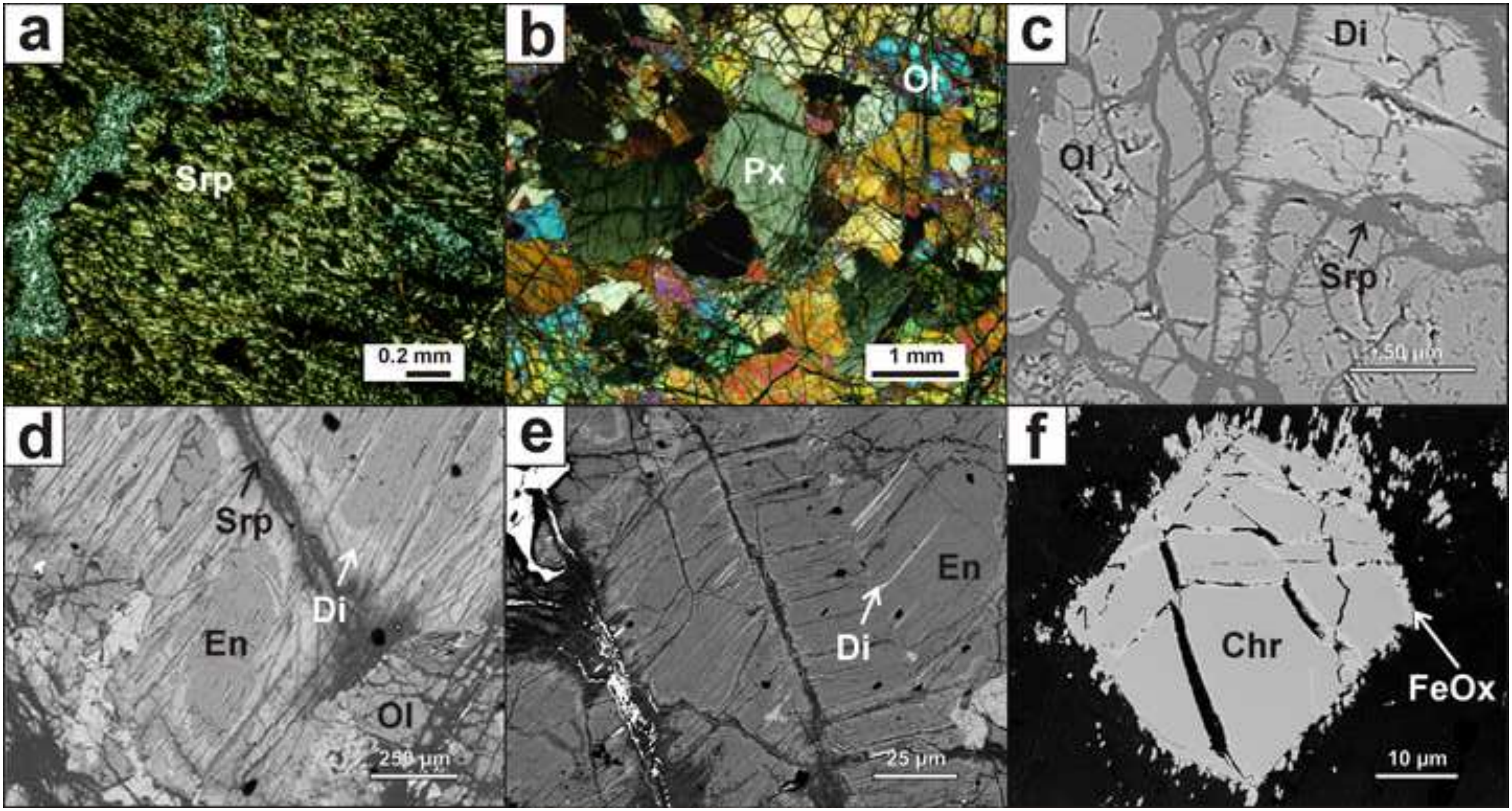
a
Srp
0.2 mm
b
Ol
Px
1 mm
c
Di
Ol
Srp
50 μm
d
Srp
Di
En
Ol
250 μm
e
En
Di
25 μm
f
Chr
FeOx
10 μm

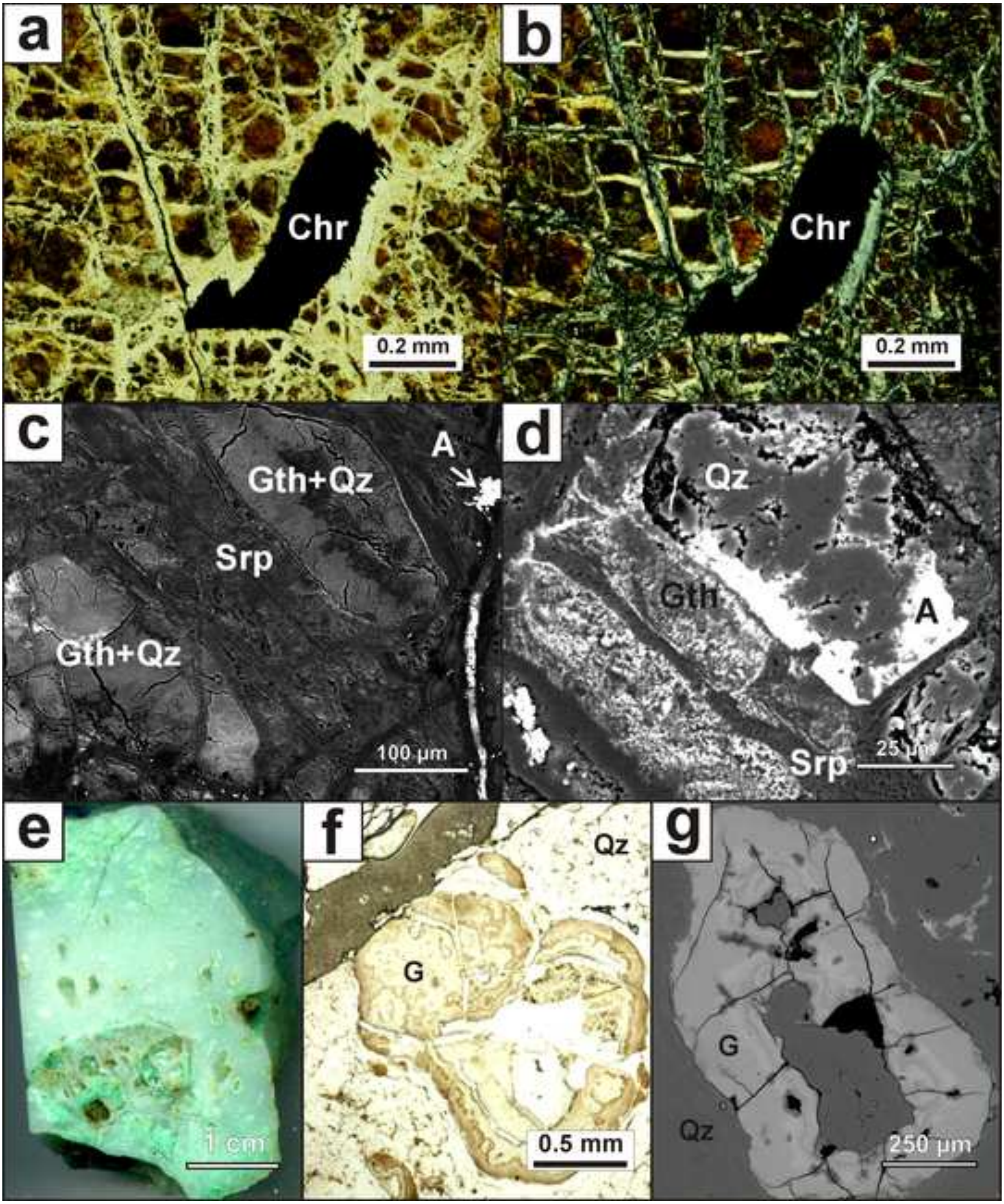
a
Chr
0.2 mm
b
Chr
0.2 mm
c
A
Gth+Qz
Srp
Gth+Qz
100 µm
d
Qz
Gth
A
Srp
25 µm
e
1 cm
f
Qz
G
0.5 mm
g
G
Qz
250 µm

Figure 8

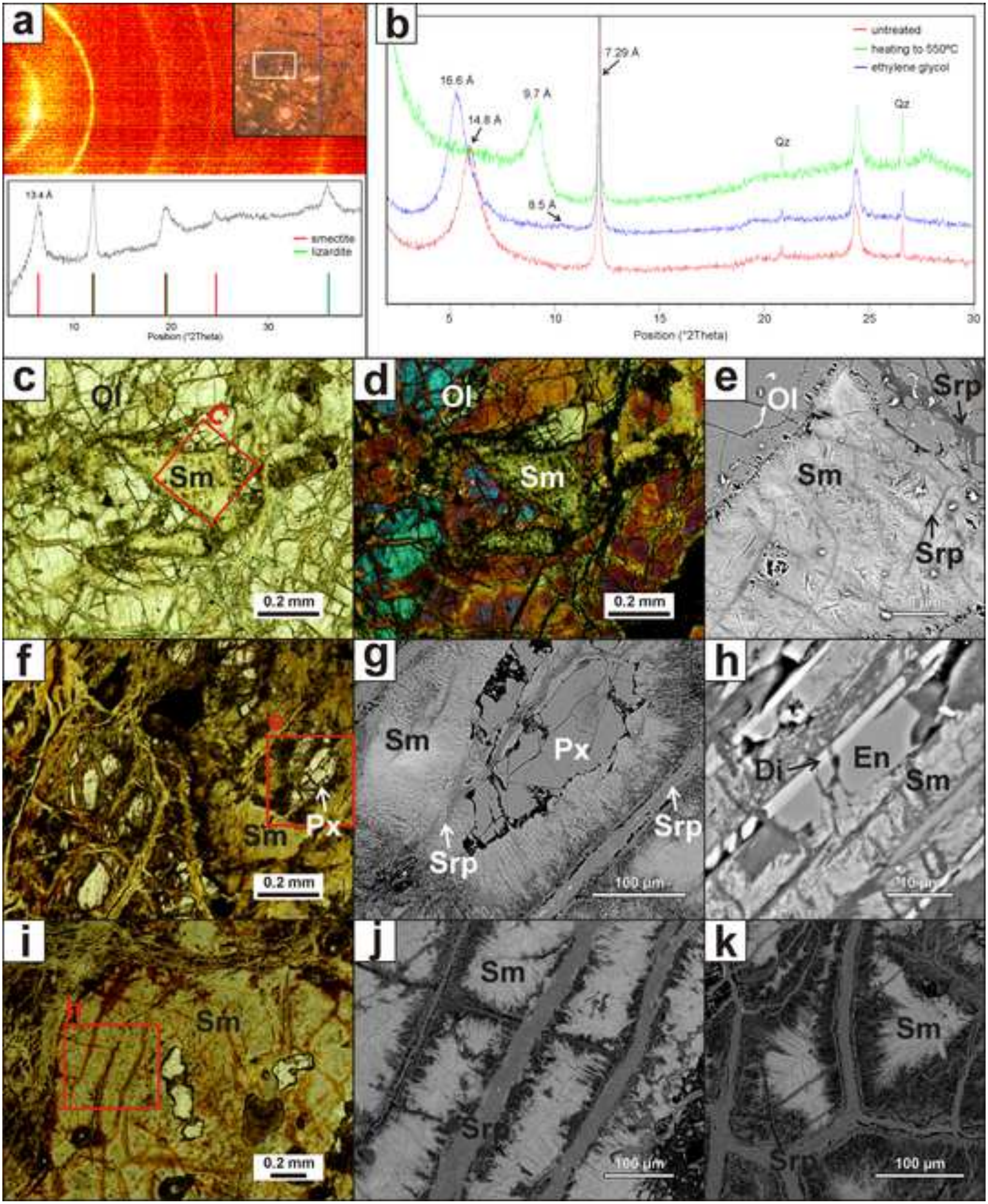
a
13.4 Å
smectite
lizardite
10
20
30
Position (°2Theta)
b
untreated
heating to 550°C
ethylene glycol
7.29 Å
16.6 Å
9.7 Å
14.8 Å
8.5 Å
Qz
Qz
5
10
15
20
25
30
Position (°2Theta)
c
Ol
Sm
c
0.2 mm
d
Ol
Sm
0.2 mm
e
Ol
Srp
Sm
Srp
10 µm
f
e
Px
Sm
0.2 mm
g
Sm
Px
Srp
Srp
100 µm
h
Di
En
Sm
10 µm
i
H
Sm
0.2 mm
j
Sm
Srp
100 µm
k
Sm
Srp
100 µm

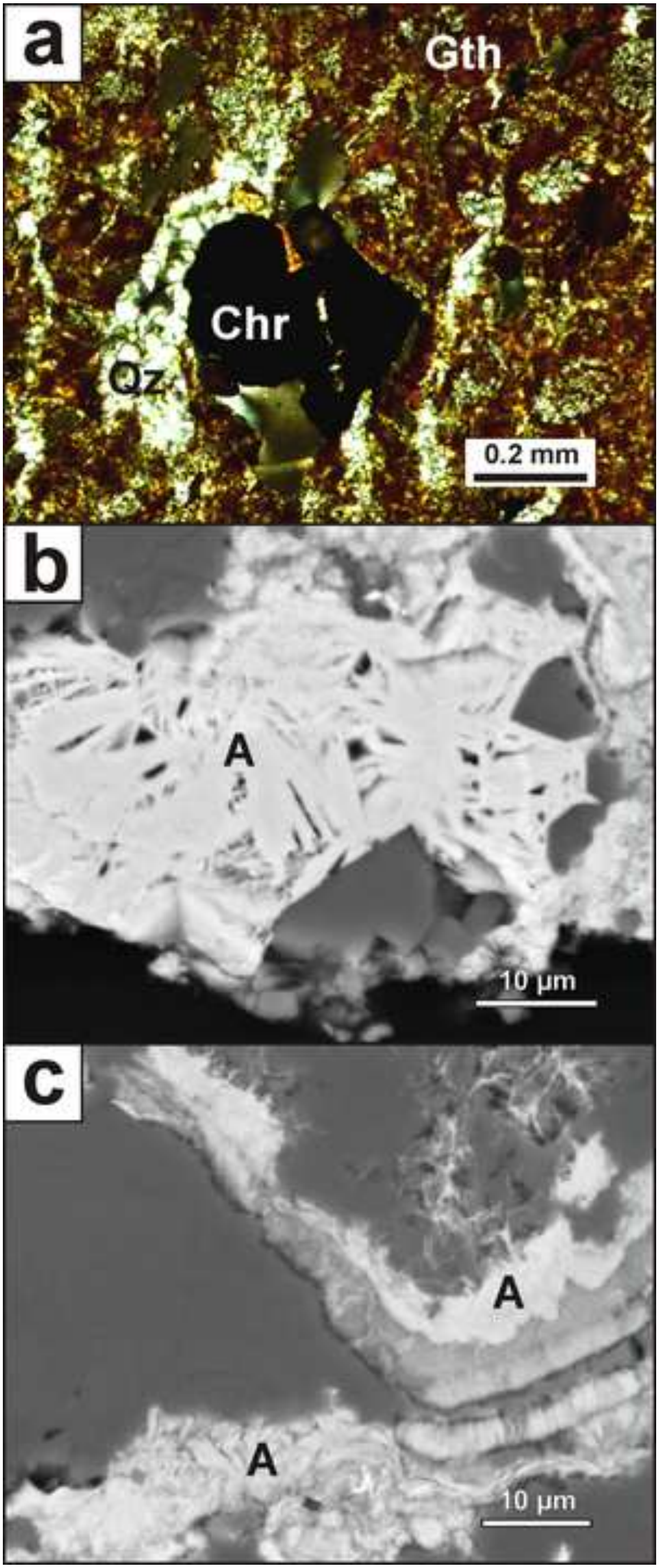
a
Gth
Chr
Qz
0.2 mm
b
A
10 µm
c
A
A
10 µm

Figure 10

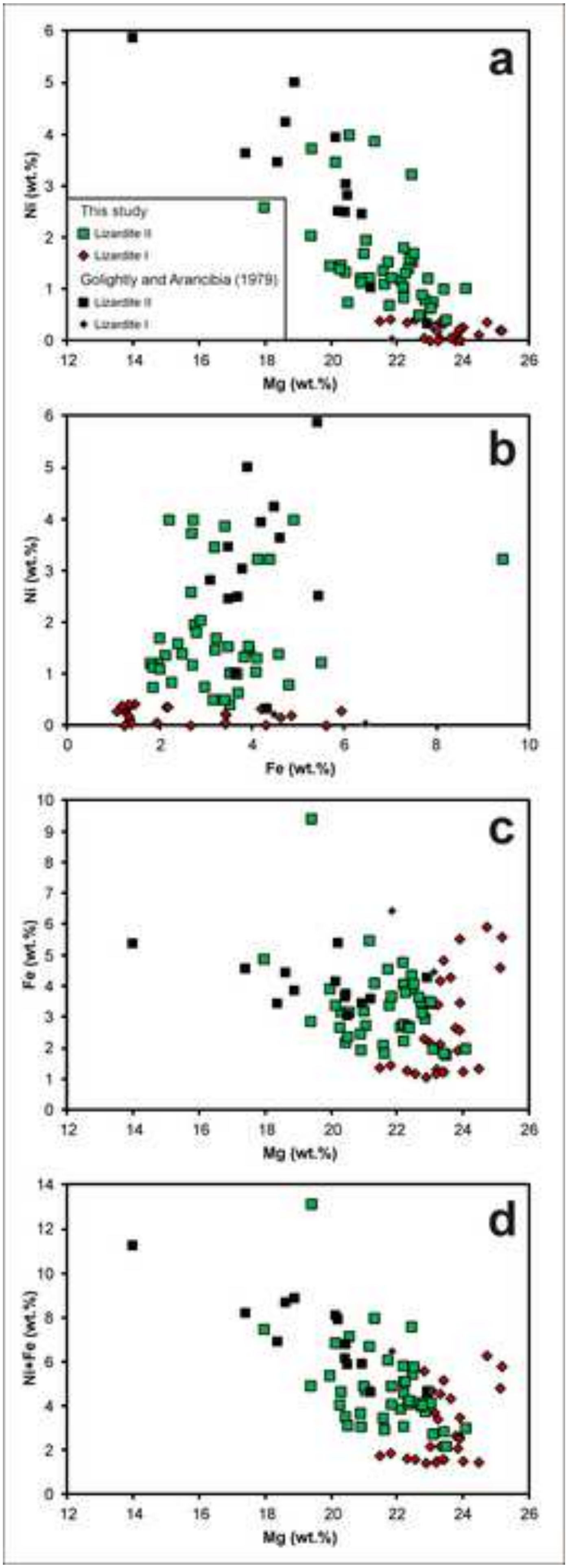
a
Ni (wt.%)
0
1
2
3
4
5
6
Mg (wt.%)
12
14
16
18
20
22
24
26
This study
🟩 Lizardite II
◆ Lizardite I
Golightly and Arancibia (1979)
■ Lizardite II
◆ Lizardite I
b
Ni (wt.%)
Fe (wt.%)
0
2
4
6
8
10
c
Fe (wt.%)
0
1
2
3
4
5
6
7
8
9
10
Mg (wt.%)
d
Ni+Fe (wt.%)
0
2
4
6
8
10
12
14
Mg (wt.%)

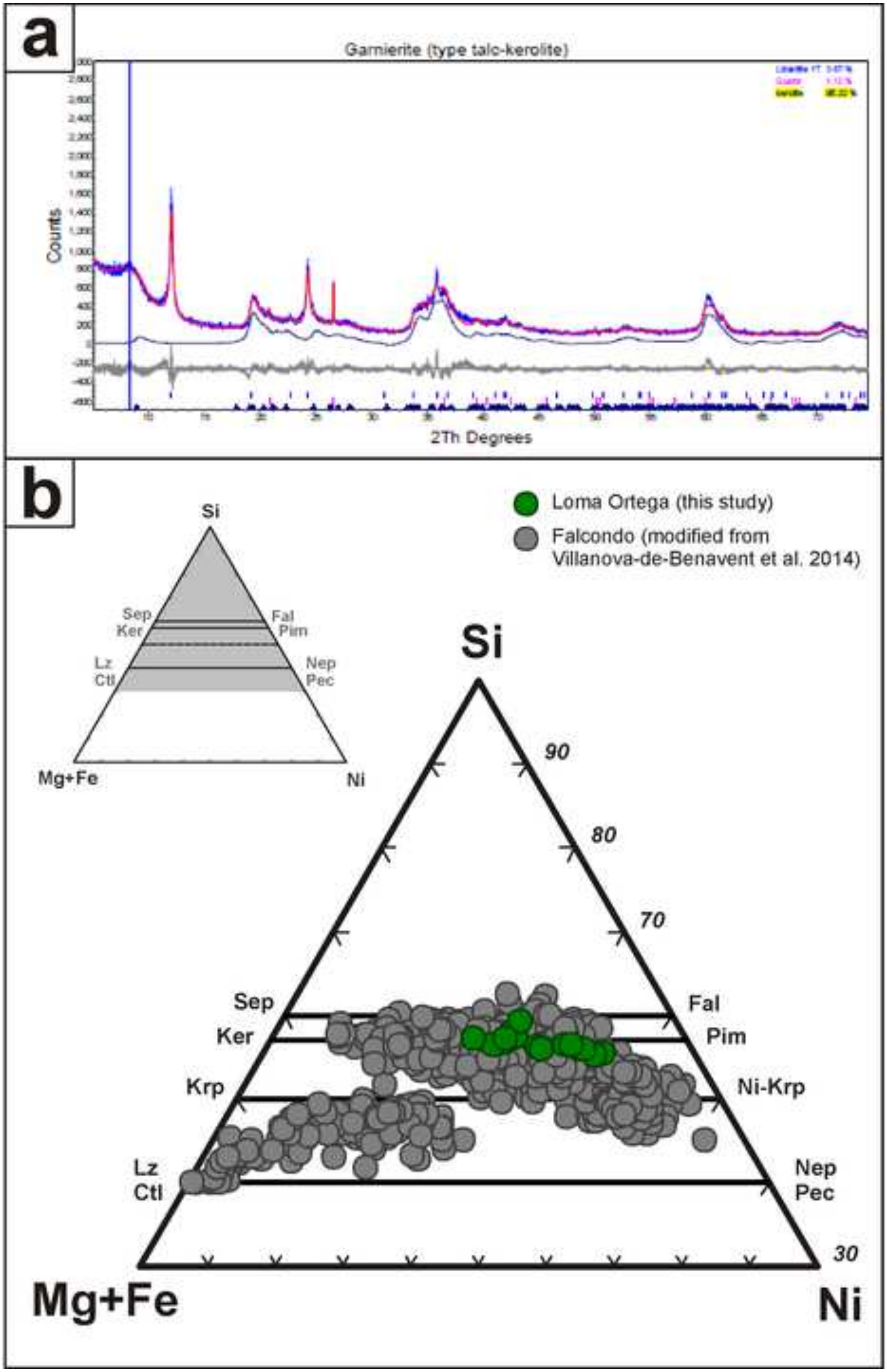
a
Garnierite (type talc-kerolite)
Counts
2,800
2,600
2,400
2,200
2,000
1,800
1,600
1,400
1,200
1,000
800
600
400
200
0
-200
-400
-600
2Th Degrees
b
Si
Sep
Ker
Fal
Pim
Lz
Ctl
Nep
Pec
Mg+Fe
Ni
Loma Ortega (this study)
Falcondo (modified from Villanova-de-Benavent et al. 2014)
Si
90
80
70
30
Sep
Ker
Krp
Lz
Ctl
Fal
Pim
Ni-Krp
Nep
Pec
Mg+Fe
Ni

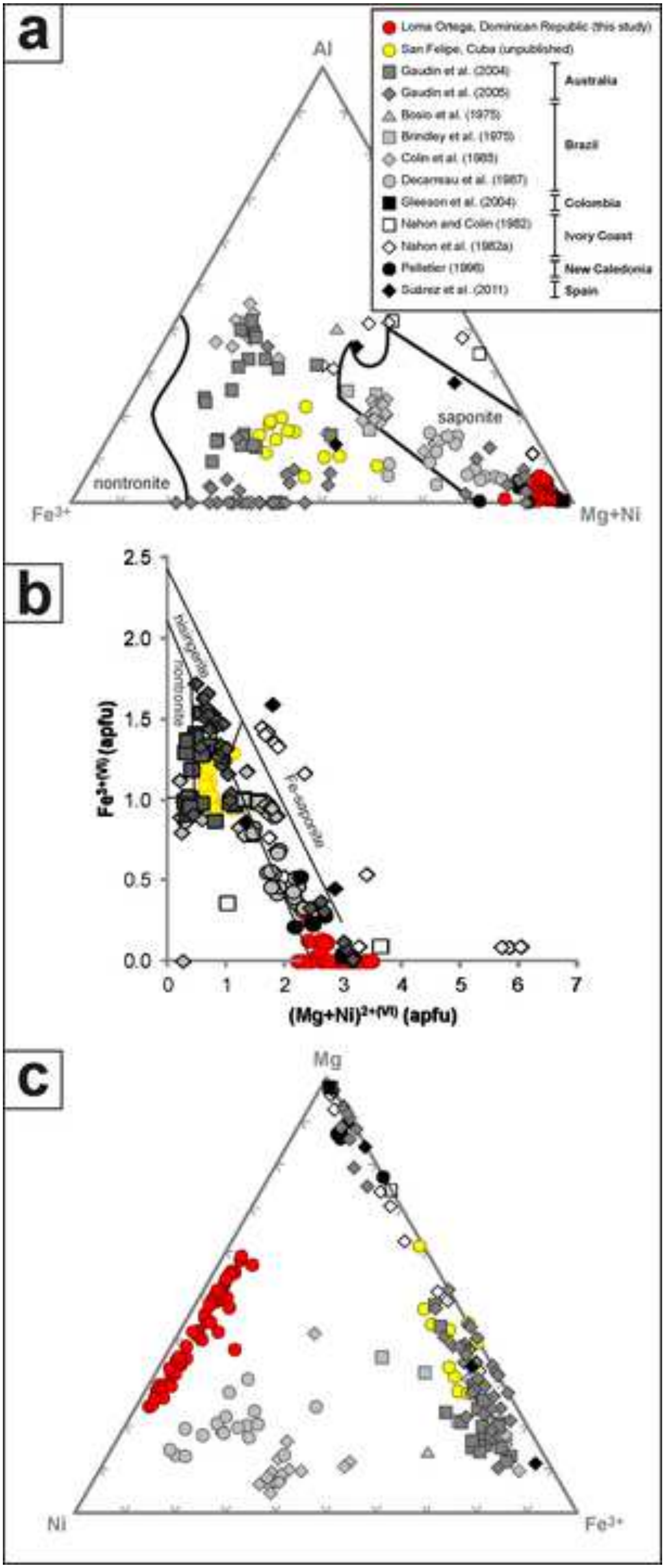
a
Al
Loma Ortega, Dominican Republic (this study)
San Felipe, Cuba (unpublished)
Gaudin et al. (2004)
Gaudin et al. (2005)
Bosio et al. (1975)
Brindley et al. (1975)
Colin et al. (1985)
Decarreau et al. (1987)
Gleeson et al. (2004)
Nahon and Colin (1982)
Nahon et al. (1982a)
Pelletier (1996)
Suárez et al. (2011)
Australia
Brazil
Colombia
Ivory Coast
New Caledonia
Spain
nontronite
saponite
Fe³⁺
Mg+Ni
b
2.5
2.0
1.5
1.0
0.5
0.0
Fe³⁺⁽ⱽᴵ⁾ (apfu)
hisingerite
nontronite
Fe-saponite
0
1
2
3
4
5
6
7
(Mg+Ni)²⁺⁽ⱽᴵ⁾ (apfu)
c
Mg
Ni
Fe³⁺

Figure 13

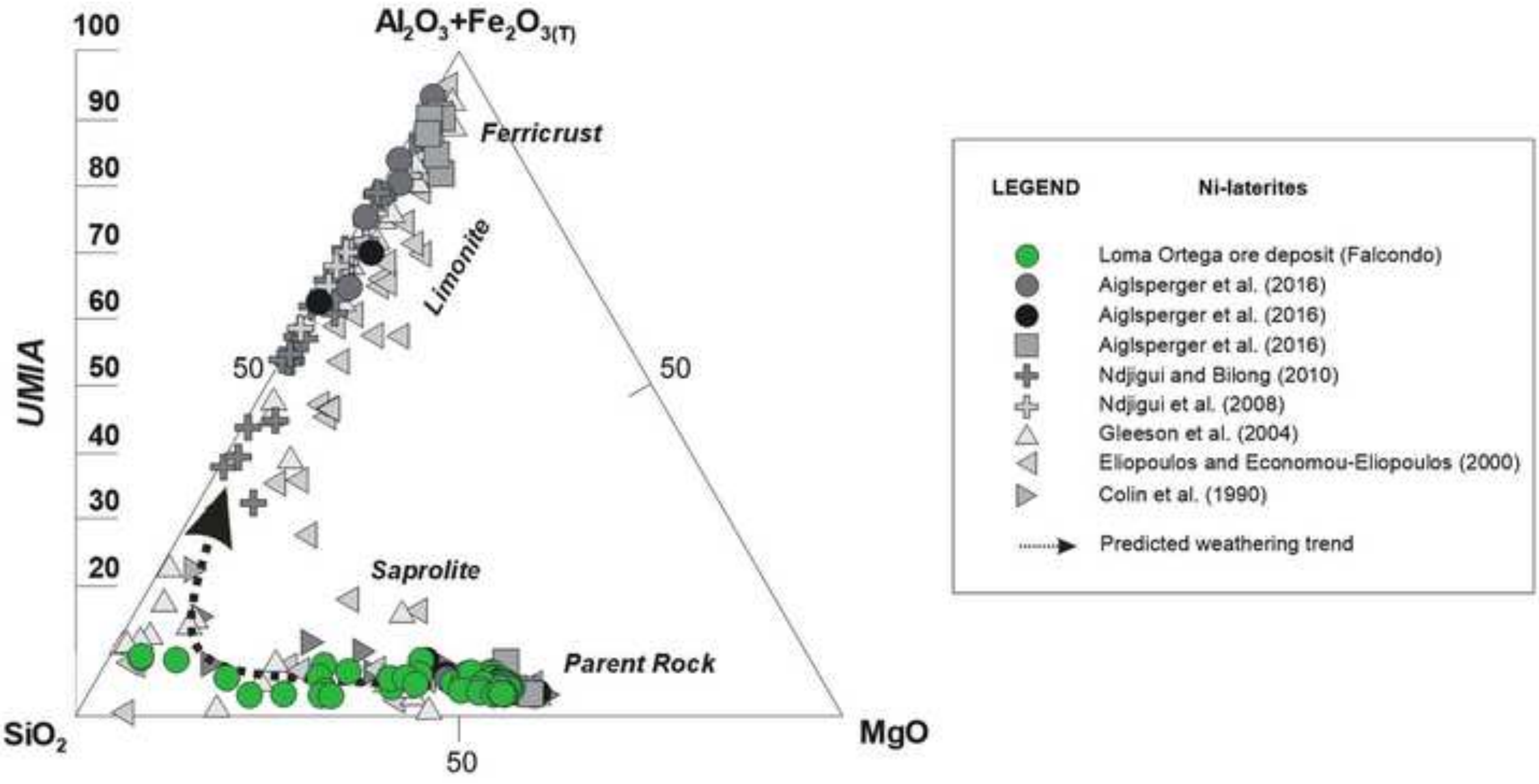
Al$_2$O$_3$+Fe$_2$O$_{3(T)}$
UMIA
100
90
80
70
60
50
40
30
20
Ferricrust
Limonite
Saprolite
Parent Rock
50
50
50
SiO$_2$
MgO
LEGEND
Ni-laterites
● Loma Ortega ore deposit (Falcondo)
● Aiglsperger et al. (2016)
● Aiglsperger et al. (2016)
■ Aiglsperger et al. (2016)
✚ Ndjigui and Bilong (2010)
✚ Ndjigui et al. (2008)
△ Gleeson et al. (2004)
◁ Eliopoulos and Economou-Eliopoulos (2000)
▷ Colin et al. (1990)
Predicted weathering trend

Table 1

| **depth [m]** | **$SiO_2$** | **$Al_2O_3$** | **$Fe_2O_3$** | **MgO** | **Ni** | **UMIA** |
|---|---|---|---|---|---|---|
| 0.00 | 67.53 | 0.82 | 17.07 | 2.11 | 0.52 | 8.9 |
| 0.50 | 68.21 | 0.79 | 17.95 | 2.08 | 0.50 | 9.2 |
| 1.00 | 65.41 | 0.64 | 17.14 | 4.70 | 0.69 | 8.6 |
| 1.65 | 67.93 | 0.60 | 12.81 | 9.89 | 0.75 | 5.9 |
| 2.40 | 44.07 | 0.86 | 18.36 | 23.82 | 2.62 | 8.5 |
| 2.95 | 42.35 | 1.61 | 10.72 | 31.08 | 2.27 | 5.3 |
| 3.55 | 55.08 | 0.66 | 16.86 | 16.54 | 1.29 | 7.8 |
| 4.55 | 40.48 | 0.70 | 12.17 | 31.20 | 2.73 | 5.4 |
| 5.00 | 46.04 | 0.67 | 14.13 | 24.83 | 1.94 | 6.4 |
| 5.35 | 40.51 | 0.71 | 11.41 | 29.63 | 2.68 | 5.3 |
| 6.05 | 52.96 | 0.68 | 14.76 | 18.74 | 1.74 | 6.9 |
| 6.65 | 40.17 | 0.72 | 11.23 | 30.15 | 2.93 | 5.2 |
| 6.85 | 40.68 | 1.41 | 10.03 | 31.58 | 0.27 | 5.0 |
| 7.00 | 42.43 | 0.73 | 9.99 | 31.96 | 2.21 | 4.4 |
| 7.50 | 53.32 | 0.69 | 10.45 | 24.61 | 1.54 | 4.6 |
| 8.00 | 43.49 | 0.65 | 9.70 | 30.63 | 2.25 | 4.3 |
| 8.30 | 49.25 | 0.67 | 12.54 | 22.49 | 1.72 | 5.8 |
| 8.55 | 44.99 | 0.71 | 11.20 | 32.89 | 1.74 | 4.7 |
| 8.70 | 44.63 | 0.71 | 11.60 | 28.96 | 2.56 | 5.2 |
| 8.90 | 48.75 | 0.65 | 13.26 | 24.25 | 1.82 | 6.0 |
| 9.00 | 41.92 | 0.91 | 11.50 | 28.98 | 2.89 | 5.4 |
| 9.10 | 39.88 | 0.70 | 9.75 | 34.58 | 1.24 | 4.3 |
| 9.35 | 41.26 | 0.77 | 11.57 | 31.19 | 2.78 | 5.2 |
| 9.60 | 41.66 | 0.70 | 11.58 | 31.96 | 2.23 | 5.1 |
| 10.65 | 41.80 | 0.73 | 12.05 | 32.05 | 2.10 | 5.3 |
| 11.00 | 41.57 | 0.70 | 10.72 | 34.22 | 2.05 | 4.6 |
| 11.15 | 43.29 | 0.71 | 10.64 | 32.31 | 2.13 | 4.6 |
| 11.40 | 43.50 | 1.13 | 10.47 | 32.39 | 2.27 | 4.8 |
| 11.80 | 40.00 | 1.68 | 10.75 | 34.13 | 2.01 | 5.3 |
| 12.25 | 39.50 | 1.80 | 10.74 | 30.90 | 1.91 | 5.6 |
| 12.45 | 39.68 | 1.73 | 10.66 | 34.36 | 1.99 | 5.2 |
| 12.65 | 42.91 | 0.91 | 9.12 | 33.66 | 3.16 | 4.1 |
| 13.00 | 39.35 | 0.98 | 10.13 | 35.45 | 0.98 | 4.5 |
| 13.50 | 43.08 | 0.94 | 12.93 | 33.23 | 1.38 | 5.5 |
| 14.30 | 40.70 | 0.82 | 11.41 | 34.04 | 1.15 | 5.0 |
| 14.55 | 45.24 | 1.00 | 11.91 | 31.98 | 1.19 | 5.2 |
| 14.70 | 41.24 | 0.83 | 10.50 | 35.02 | 0.83 | 4.5 |
| 15.60 | 45.05 | 0.94 | 12.48 | 31.21 | 1.06 | 5.4 |
| 16.00 | 42.18 | 1.12 | 13.28 | 30.17 | 1.31 | 6.1 |
| 16.30 | 39.10 | 1.64 | 13.97 | 31.35 | 1.18 | 6.8 |
| 16.50 | 38.99 | 1.52 | 12.80 | 31.65 | 1.33 | 6.2 |
| 16.70 | 42.36 | 2.00 | 13.59 | 30.38 | 0.96 | 6.7 |
| 16.80 | 40.86 | 1.63 | 11.93 | 34.78 | 0.95 | 5.6 |
| 17.00 | 41.30 | 2.06 | 13.91 | 33.66 | 0.97 | 6.6 |
| 17.15 | 40.50 | 1.98 | 11.99 | 33.03 | 1.09 | 6.0 |
| 17.45 | 40.78 | 1.88 | 10.58 | 32.76 | 1.15 | 5.4 |

| | | | | | | |
|---|---|---|---|---|---|---|
| 17.55 | 40.63 | 1.83 | 11.68 | 32.83 | 1.17 | 5.8 |
| 17.80 | 39.81 | 1.46 | 9.89 | 35.10 | 0.64 | 4.7 |
| 18.20 | 40.71 | 1.38 | 12.54 | 34.70 | 0.97 | 5.6 |
| 18.55 | 39.50 | 1.35 | 11.19 | 32.89 | 0.89 | 5.4 |
| 18.70 | 39.26 | 1.74 | 9.89 | 34.05 | 0.68 | 5.0 |
| 19.10 | 40.76 | 2.24 | 10.06 | 34.10 | 0.83 | 5.3 |
| 19.40 | 39.86 | 1.66 | 10.30 | 34.81 | 0.59 | 5.0 |
| 19.70 | 40.13 | 1.70 | 10.01 | 34.08 | 0.69 | 5.0 |
| 20.00 | 40.31 | 1.51 | 10.49 | 35.72 | 0.34 | 4.9 |
| 20.40 | 40.71 | 1.70 | 10.07 | 35.55 | 0.30 | 4.9 |
| 21.35 | 40.17 | 1.66 | 10.63 | 34.49 | 0.37 | 5.2 |
| 22.25 | 41.35 | 1.44 | 11.01 | 36.18 | 0.35 | 5.0 |
| 23.50 | 40.24 | 1.48 | 10.87 | 33.90 | 0.38 | 5.2 |
| 23.90 | 42.70 | 1.04 | 10.59 | 34.98 | 0.36 | 4.6 |
| 24.25 | 40.78 | 1.05 | 10.40 | 35.67 | 0.33 | 4.6 |
| 24.50 | 45.12 | | 11.13 | 13.34 | 0.47 | 6.1 |
| 25.10 | 41.36 | 1.39 | 10.66 | 35.90 | 0.32 | 4.8 |
| 25.50 | 41.53 | 1.16 | 10.38 | 33.74 | 1.22 | 4.8 |
| 26.00 | 40.93 | 1.34 | 10.46 | 34.98 | 0.38 | 4.8 |
| 26.65 | 41.70 | 1.30 | 11.29 | 35.67 | 0.38 | 5.0 |
| 27.25 | 41.07 | 1.13 | 10.25 | 34.53 | 0.33 | 4.7 |
| 27.40 | 39.49 | 0.79 | 8.75 | 33.48 | 0.31 | 4.0 |
| 27.60 | 44.12 | 0.72 | 10.66 | 36.67 | 0.34 | 4.3 |
| 28.10 | 42.78 | 0.78 | 10.06 | 36.84 | 0.38 | 4.2 |
| 28.25 | 42.35 | 1.10 | 8.81 | 37.62 | 0.34 | 3.9 |
| 28.85 | 41.67 | 1.11 | 9.64 | 36.68 | 0.41 | 4.3 |
| 28.95 | 43.75 | 0.84 | 11.88 | 33.50 | 0.49 | 5.0 |
| 29.30 | 42.57 | 1.40 | 9.50 | 35.85 | 0.40 | 4.4 |
| 29.60 | 46.63 | 1.06 | 10.07 | 34.85 | 0.30 | 4.3 |
| 32.60 | 48.79 | 0.71 | 9.80 | 33.09 | 0.32 | 4.0 |
| 32.70 | 46.68 | 0.73 | 9.03 | 34.99 | 0.30 | 3.7 |
| 33.75 | 43.23 | 0.76 | 8.51 | 37.43 | 0.29 | 3.6 |
| 34.35 | 44.89 | 0.73 | 8.11 | 36.35 | 0.29 | 3.4 |
| 34.75 | 44.05 | 0.74 | 8.82 | 36.72 | 0.29 | 3.7 |
| 35.05 | 42.73 | 0.72 | 8.01 | 36.66 | 0.27 | 3.4 |
| 35.90 | 43.60 | 0.75 | 8.38 | 37.01 | 0.29 | 3.5 |

Table 2

| depth [m] | Os | Ir | Ru | Rh | Pt | Pd |
|---|---|---|---|---|---|---|
| 0.50 | 6 | 7 | 9 | 3 | 20 | 4 |
| 5.00 | 13 | 12 | 21 | 4 | 21 | 4 |
| 8.00 | 7 | 7 | 13 | 3 | 12 | 3 |
| 11.00 | 5 | 4 | 9 | 2 | 8 | 3 |
| 28.10 | 4 | 4 | 7 | 1 | 8 | 4 |
| 35.05 | 3 | 3 | 9 | 1 | 6 | 3 |

| **Σ PGE** | **IPGE/PPGE** |
|---:|---:|
| 49 | 0.81 |
| 75 | 1.59 |
| 45 | 1.50 |
| 31 | 1.38 |
| 28 | 1.15 |
| 25 | 1.50 |

Table 3

| | Olivine | Olivine | Olivine | Olivine | Olivine | Olivine | Enstatite | Enstatite | Enstatite | Enstatite | Enstatite |
|---|---|---|---|---|---|---|---|---|---|---|---|
| Label | lo53ol4 | lo53ol6 | Lo53Af36 | lo53B8 | lo53B10 | Lo1811 | lo53f2 | lo53f21 | lo53f24 | lo53Bpx2 | lo53Bpx3 |
| $SiO_2$ | 39.09 | 40.87 | 39 | 40.54 | 39.71 | 41.64 | 55.33 | 55.28 | 55.25 | 56.88 | 56.89 |
| $TiO_2$ | 0 | 0 | 0.02 | 0 | 0 | 0 | 0.02 | 0.02 | 0.01 | 0.03 | 0.02 |
| $Al_2O_3$ | 0.03 | 0 | 0 | 0 | 0.02 | 0 | 2.46 | 2.36 | 2.4 | 2.76 | 2.66 |
| $Cr_2O_3$ | 0.01 | 0 | 0 | 0 | 0.01 | 0.01 | 0.64 | 0.64 | 0.71 | 0.54 | 0.51 |
| FeO | 8.74 | 9.51 | 9.54 | 9.48 | 9.56 | 8.05 | 5.45 | 5.65 | 5.81 | 5.77 | 6.02 |
| MnO | 0.10 | 0.16 | 0.13 | 0.08 | 0.10 | 0.09 | 0.16 | 0.08 | 0.12 | 0.13 | 0.11 |
| MgO | 51.08 | 49.41 | 50.11 | 49.41 | 49.59 | 49.98 | 32.86 | 33.68 | 33.95 | 33.88 | 34.24 |
| NiO | 0.53 | 0.38 | 0.47 | 0.35 | 0.38 | 0.33 | 0.11 | 0.14 | 0.07 | 0 | 0 |
| CaO | 0.03 | 0.01 | 0.01 | 0.05 | 0.04 | 0.02 | 2.06 | 1.19 | 1.51 | 0.64 | 0.44 |
| $Na_2O$ | 0 | 0 | 0 | 0.03 | 0 | 0.02 | 0 | 0 | 0 | 0 | 0.03 |
| $K_2O$ | 0 | 0 | 0 | 0 | 0 | 0 | 0 | 0 | 0 | 0 | 0 |
| Total Ox | 99.6 | 100.35 | 99.27 | 99.93 | 99.41 | 100.14 | 99.09 | 99.03 | 99.84 | 100.64 | 100.92 |
| | | | | | | | | | | | |
| Si | 1.885 | 1.949 | 1.889 | 1.941 | 1.916 | 1.980 | 1.884 | 1.883 | 1.871 | 1.891 | 1.891 |
| Ti | 0.000 | 0.000 | 0.001 | 0.000 | 0.000 | 0.000 | 0.001 | 0.001 | 0.000 | 0.001 | 0.000 |
| Al | 0.002 | 0.000 | 0.000 | 0.000 | 0.001 | 0.000 | 0.197 | 0.189 | 0.192 | 0.216 | 0.208 |
| Cr | 0.000 | 0.000 | 0.000 | 0.000 | 0.000 | 0.000 | 0.017 | 0.017 | 0.019 | 0.014 | 0.013 |
| Fe | 0.352 | 0.379 | 0.386 | 0.380 | 0.386 | 0.320 | 0.155 | 0.161 | 0.165 | 0.160 | 0.167 |
| Mn | 0.004 | 0.006 | 0.005 | 0.003 | 0.004 | 0.004 | 0.004 | 0.002 | 0.003 | 0.003 | 0.003 |
| Mg | 3.672 | 3.512 | 3.617 | 3.527 | 3.567 | 3.542 | 1.668 | 1.710 | 1.714 | 1.679 | 1.696 |
| Ni | 0.021 | 0.015 | 0.018 | 0.013 | 0.015 | 0.013 | 0.003 | 0.004 | 0.002 | 0.000 | 0.000 |
| Ca | 0.002 | 0.001 | 0.001 | 0.003 | 0.002 | 0.001 | 0.075 | 0.043 | 0.055 | 0.023 | 0.016 |
| Na | 0.000 | 0.000 | 0.000 | 0.003 | 0.000 | 0.002 | 0.000 | 0.000 | 0.000 | 0.000 | 0.002 |
| K | 0.000 | 0.000 | 0.000 | 0.000 | 0.000 | 0.000 | 0.001 | 0.001 | 0.000 | 0.001 | 0.000 |
| | | | | | | | | | | | |
| Fo | 91.24 | 90.25 | 90.35 | 90.28 | 90.24 | 91.71 | | | | | |
| En | | | | | | | 87.87 | 89.33 | 88.66 | 90.16 | 90.26 |
| Wo | | | | | | | 3.96 | 2.27 | 2.83 | 1.22 | 0.83 |

| Enstatite | Diopside | Diopside | Diopside | Diopside | Diopside | Diopside |
|---|---|---|---|---|---|---|
| lo53Bpx4 | lo53Bpx8v | LO-18,5_2px2 | lo53B9 | lo5px1 | lo5px3 | lo5px2 |
| 55.62 | 54.4 | 53.71 | 53.44 | 53.11 | 53.18 | 52.71 |
| 0 | 0 | 0.05 | 0.01 | 0.01 | 0.06 | 0.04 |
| 2.62 | 1.3 | 1.81 | 2.28 | 2.48 | 2.38 | 2.59 |
| 0.51 | 0.42 | 0.77 | 0.6 | 0.88 | 0.81 | 0.94 |
| 5.93 | 1.63 | 1.46 | 2.25 | 2.21 | 2.11 | 2.2 |
| 0.13 | 0.1 | 0.07 | 0.06 | 0.08 | 0.16 | 0.08 |
| 34.37 | 18.47 | 20.48 | 17.83 | 17.68 | 17.25 | 17.11 |
| 0 | 0.00 | 0.08 | 0.1 | 0.00 | 0.00 | 0 |
| 0.83 | 23.03 | 21.5 | 23.63 | 23.76 | 24.03 | 24.04 |
| 0.04 | 0.2 | 0.23 | 0.05 | 0.02 | 0.04 | 0 |
| 0 | 0 | 0 | 0.01 | 0 | 0 | 0 |
| 100.05 | 99.55 | 100.16 | 100.26 | 100.22 | 100.02 | 99.71 |
|  |  |  |  |  |  |  |
| 1.871 | 1.945 | 1.895 | 1.890 | 1.876 | 1.884 | 1.871 |
| 0.000 | 0.000 | 0.001 | 0.000 | 0.000 | 0.002 | 0.001 |
| 0.208 | 0.110 | 0.151 | 0.190 | 0.207 | 0.199 | 0.217 |
| 0.014 | 0.012 | 0.021 | 0.017 | 0.025 | 0.023 | 0.026 |
| 0.167 | 0.049 | 0.043 | 0.067 | 0.065 | 0.063 | 0.065 |
| 0.003 | 0.002 | 0.002 | 0.001 | 0.002 | 0.004 | 0.002 |
| 1.723 | 0.985 | 1.077 | 0.940 | 0.931 | 0.911 | 0.906 |
| 0.000 | 0.000 | 0.002 | 0.003 | 0.000 | 0.000 | 0.000 |
| 0.030 | 0.882 | 0.813 | 0.895 | 0.899 | 0.912 | 0.914 |
| 0.003 | 0.014 | 0.016 | 0.003 | 0.001 | 0.003 | 0.000 |
| 0.000 | 0.000 | 0.000 | 0.000 | 0.000 | 0.000 | 0.000 |
|  |  |  |  |  |  |  |
| 89.76 |  |  |  |  |  |  |
| 1.56 |  |  |  |  |  |  |

Table 4

| Mineral | Serpentine I | Serpentine I | Serpentine I | Serpentine I | Serpentine I | Serpentine II | Serpentine II | Serpentine II |
|---|---|---|---|---|---|---|---|---|
| Label | LO-18,5_37 | lo555 | lo557 | lo551 | lo553 | LO-52 A 14 | LO-52 A 16 | LO-52 A 13 |
| Depth (m) | 18.5 | 41 | 41 | 41 | 41 | 8 | 8 | 8 |
| $SiO_2$ | 42.75 | 44.03 | 44.08 | 44.17 | 41.09 | 41.14 | 40.82 | 41.01 |
| $TiO_2$ | 0.00 | 0.01 | 0.02 | 0.00 | 0.02 | 0.00 | 0.02 | 0.00 |
| $Al_2O_3$ | 1.48 | 0.11 | 0.03 | 0.01 | 0.01 | 0.01 | 0.00 | 0.00 |
| $Cr_2O_3$ | 0.30 | 0.23 | 0.14 | 0.08 | 0.17 | na | na | na |
| FeOx(*) | 2.75 | 1.73 | 1.70 | 1.65 | 1.87 | 5.01 | 5.02 | 4.23 |
| MnO | 0.03 | 0.06 | 0.11 | 0.38 | 0.44 | 0.06 | 0.04 | 0.09 |
| MgO | 38.62 | 40.56 | 38.45 | 36.96 | 36.13 | 38.14 | 37.71 | 37.55 |
| NiO | 0.05 | 0.15 | 0.23 | 0.45 | 0.53 | 0.64 | 0.81 | 1.01 |
| CaO | 0.52 | 0.04 | 0.07 | 0.04 | 0.07 | 0.03 | 0.02 | 0.04 |
| Total Ox | 86.53 | 86.96 | 84.85 | 83.81 | 80.43 | 84.56 | 83.98 | 83.52 |
| (*) FeO in Serp I, $Fe_2O_3$ Serp II | | | | | | | | |
| | | | | | | | | |
| Si | 1.993 | 2.036 | 2.082 | 2.113 | 2.062 | 1.980 | 1.981 | 1.998 |
| Ti | 0.000 | 0.000 | 0.001 | 0.000 | 0.001 | 0.000 | 0.001 | 0.000 |
| Al | 0.081 | 0.006 | 0.002 | 0.001 | 0.001 | 0.001 | 0.000 | 0.000 |
| Cr | 0.011 | 0.008 | 0.005 | 0.003 | 0.007 | | | |
| Fe | 0.107 | 0.067 | 0.067 | 0.066 | 0.078 | 0.182 | 0.183 | 0.155 |
| Mn | 0.001 | 0.002 | 0.004 | 0.015 | 0.019 | 0.002 | 0.002 | 0.004 |
| Mg | 2.685 | 2.796 | 2.707 | 2.635 | 2.702 | 2.737 | 2.728 | 2.727 |
| Ni | 0.002 | 0.006 | 0.009 | 0.017 | 0.021 | 0.025 | 0.032 | 0.040 |
| Ca | 0.026 | 0.002 | 0.004 | 0.002 | 0.004 | 0.002 | 0.001 | 0.002 |

| | | | | | | |
|---|---|---|---|---|---|---|
| Serpentine II | Serpentine II | Serpentine II | Serpentine II | Serpentine II | Serpentine II | Serpentine II |
| LO-52 A 17 | Lo53Afractura11 | lo53Afractura2 | lo53Bliz2 | lo53B28 | lo53Bliz10 | lo53Bliz3 |
| 8 | 17 | 17 | 18 | 18 | 18 | 18 |
| 40.87 | 40.94 | 40.21 | 42.52 | 41.89 | 42.49 | 42.90 |
| 0.02 | 0.00 | 0.01 | 0.00 | 0.01 | 0.03 | 0.01 |
| 0.00 | 1.01 | 1.30 | 0.50 | 2.61 | 3.02 | 1.79 |
| na | na | na | 0.09 | 0.00 | 0.03 | 0.04 |
| 6.83 | 3.53 | 3.13 | 5.61 | 4.59 | 3.98 | 3.92 |
| 0.16 | 0.00 | 0.02 | 0.09 | 0.00 | 0.03 | 0.04 |
| 36.06 | 37.29 | 37.02 | 33.07 | 33.63 | 34.78 | 34.88 |
| 1.33 | 1.54 | 1.70 | 1.86 | 2.16 | 2.30 | 2.49 |
| 0.03 | 0.01 | 0.04 | 0.09 | 0.25 | 0.14 | 0.09 |
| 84.65 | 84.15 | 83.31 | 83.32 | 85.36 | 86.60 | 86.19 |
| | | | | | | |
| 1.980 | 1.983 | 1.970 | 2.077 | 2.012 | 1.999 | 2.035 |
| 0.001 | 0.000 | 0.000 | 0.000 | 0.000 | 0.001 | 0.000 |
| 0.000 | 0.058 | 0.075 | 0.029 | 0.148 | 0.167 | 0.100 |
| | | | 0.003 | 0.000 | 0.001 | 0.002 |
| 0.249 | 0.129 | 0.116 | 0.206 | 0.166 | 0.141 | 0.140 |
| 0.007 | 0.000 | 0.001 | 0.004 | 0.000 | 0.001 | 0.002 |
| 2.604 | 2.693 | 2.704 | 2.408 | 2.408 | 2.440 | 2.466 |
| 0.052 | 0.060 | 0.067 | 0.073 | 0.083 | 0.087 | 0.095 |
| 0.002 | 0.001 | 0.002 | 0.005 | 0.013 | 0.007 | 0.005 |

Table 5

| Label | L0-53AA-9 | L0-53AA-4 | L0-53AA-14 | L0-53AA-12 | L0-53AA-11 | L0-53AA-8 | L0-53AA-15 | L0-53AA-7 |
|---|---|---|---|---|---|---|---|---|
| Depth (m) | 16.7 | 16.7 | 16.7 | 16.7 | 16.7 | 16.7 | 16.7 | 16.7 |
| $SiO_2$ | 49.75 | 49.19 | 52.56 | 46.8 | 48.86 | 45.8 | 46.02 | 46 |
| $Al_2O_3$ | 0.14 | 0.19 | 0.64 | 0.46 | 0.46 | 0.11 | 0.38 | 0.16 |
| $Fe_2O_3$* | 0.29 | 0.19 | 0.10 | 0 | 0.08 | 0.28 | 0.06 | 0.11 |
| MgO | 12.58 | 10.96 | 9.47 | 8.72 | 9.17 | 6.18 | 5.99 | 5.06 |
| NiO | 22.93 | 26.42 | 27.73 | 29.95 | 30.37 | 33.13 | 33.92 | 36.52 |
| CaO | 0.09 | 0.1 | 0.1 | 0.09 | 0.06 | 0.09 | 0.06 | 0.11 |
| $Na_2O$ | 0.05 | 0.07 | 0.04 | 0.18 | 0.11 | 0.11 | 0.05 | 0.06 |
| $K_2O$ | 0.07 | 0.04 | 0.06 | 0.06 | 0.05 | 0.03 | 0.05 | 0.02 |
| Total Ox | 85.91 | 87.2 | 90.75 | 86.31 | 89.21 | 85.78 | 86.61 | 88.11 |
| | | | | | | | | |
| Si | 3.981 | 3.958 | 4.044 | 3.906 | 3.925 | 3.930 | 3.920 | 3.907 |
| Al | 0.013 | 0.018 | 0.058 | 0.045 | 0.044 | 0.011 | 0.038 | 0.016 |
| $Fe^{3+}$ | 0.017 | 0.011 | 0.006 | 0 | 0.005 | 0.018 | 0.004 | 0.007 |
| Mg | 1.501 | 1.315 | 1.086 | 1.085 | 1.098 | 0.791 | 0.761 | 0.641 |
| Ni | 1.476 | 1.710 | 1.716 | 2.010 | 1.962 | 2.287 | 2.324 | 2.495 |
| Ca | 0.008 | 0.009 | 0.008 | 0.008 | 0.005 | 0.008 | 0.005 | 0.010 |
| Na | 0.008 | 0.011 | 0.006 | 0.029 | 0.017 | 0.018 | 0.008 | 0.010 |
| K | 0.007 | 0.004 | 0.006 | 0.006 | 0.005 | 0.003 | 0.005 | 0.002 |
| Cations | 7.011 | 7.035 | 6.930 | 7.090 | 7.062 | 7.066 | 7.066 | 7.088 |

# Table 6

| Label | LO-9,8_1SM16 | lo53sm2 | -53A 2_esm6 | lo53sm10 | Lo53Af32 | lo53sm12 | lo53sm8 |
|---|---|---|---|---|---|---|---|
| Depth (m) | 9.8 | 16.7 | 16.7 | 16.7 | 16.7 | 16.7 | 16.7 |
| $SiO_2$ | 52.22 | 45.92 | 43.78 | 45.89 | 44.28 | 46.33 | 43.1 |
| $TiO_2$ | 0.02 | 0.02 | 0.04 | 0.03 | 0.03 | 0.01 | 0 |
| $Al_2O_3$ | 0.34 | 1.5 | 0.54 | 1.22 | 1.39 | 1.69 | 1.65 |
| $Cr_2O_3$ | 0.26 | 0.67 | 0.42 | 0.43 | 0.69 | 0.55 | 0.64 |
| $Fe_2O_3$* | 1.86 | 1.71 | 1.91 | 1.71 | 1.83 | 1.72 | 1.77 |
| MnO | 0.09 | 0 | 0.08 | 0.14 | 0.1 | 0.02 | 0.18 |
| MgO | 13.78 | 11.2 | 14.89 | 9.27 | 10.97 | 11.51 | 14.55 |
| NiO | 16.15 | 18.87 | 21.18 | 22.43 | 23.5 | 24.06 | 25.48 |
| CoO |  |  | 0.04 |  |  |  |  |
| CaO | 9.16 | 0.62 | 1.11 | 0.21 | 0.73 | 1.03 | 0.35 |
| $Na_2O$ | 0 | 0.12 | 0 | 0.02 | 0.09 | 0.12 | 0 |
| $K_2O$ | 0.02 | 0.04 | 0 | 0.01 | 0.03 | 0.03 | 0.02 |
| Total Ox | 93.75 | 82.81 | 83.8 | 84.06 | 85.6 | 86.89 | 82.96 |
|  |  |  |  |  |  |  |  |
| Si | 3.806 | 3.888 | 3.655 | 3.924 | 3.742 | 3.747 | 3.522 |
| Ti | 0.001 | 0.001 | 0.003 | 0.002 | 0.002 | 0.001 | 0 |
| Al | 0.029 | 0.150 | 0.053 | 0.123 | 0.138 | 0.161 | 0.159 |
| Cr | 0.015 | 0.045 | 0.028 | 0.029 | 0.046 | 0.035 | 0.041 |
| $Fe^{3+}$ | 0.102 | 0.109 | 0.120 | 0.110 | 0.117 | 0.105 | 0.109 |
| Mn | 0.006 | 0 | 0.006 | 0.010 | 0.007 | 0.001 | 0.012 |
| Mg | 1.497 | 1.414 | 1.853 | 1.182 | 1.382 | 1.388 | 1.773 |
| Ni | 0.947 | 1.285 | 1.422 | 1.543 | 1.597 | 1.565 | 1.675 |
| Co | 0 | 0 | 0.003 | 0 | 0 | 0 | 0 |
| Ca | 0.715 | 0.056 | 0.099 | 0.019 | 0.066 | 0.089 | 0.031 |
| Na | 0 | 0.020 | 0 | 0.003 | 0.015 | 0.019 | 0 |
| K | 0.002 | 0.004 | 0 | 0.001 | 0.003 | 0.003 | 0.002 |
| Cations | 7.120 | 6.971 | 7.242 | 6.946 | 7.115 | 7.113 | 7.324 |

| LO-9,8_1SM15 | -53A 2_esm15 | -53A 2_esm4 | -53A 2_esm | LO-9,8_1SM5 |
|---|---|---|---|---|
| 9.8 | 16.7 | 16.7 | 16.7 | 9.8 |
| 43.24 | 44.97 | 42.79 | 43.2 | 46.93 |
| 0.02 | 0.01 | 0.01 | 0.01 | 0 |
| 0.95 | 0.58 | 0.2 | 0.48 | 0.13 |
| 0.43 | 0.32 | 0.34 | 0.42 | 0.18 |
| 4.50 | 2.27 | 1.32 | 2.30 | 1.54 |
| 0.06 | 0.07 | 0.12 | 0 | 0.32 |
| 11.98 | 8.68 | 7 | 6.64 | 6.59 |
| 27.06 | 29.32 | 31.93 | 32.17 | 33.41 |
|  | 0.01 | 0.02 | 0.06 |  |
| 0.71 | 0.82 | 0.42 | 1.21 | 1.72 |
| 0.03 | 0.01 | 0.05 | 0 | 0 |
| 0.01 | 0.01 | 0.01 | 0 | 0.01 |
| 88.55 | 86.83 | 84.08 | 86.26 | 90.74 |
|  |  |  |  |  |
| 3.543 | 3.765 | 3.778 | 3.728 | 3.828 |
| 0.001 | 0.001 | 0.001 | 0.001 | 0 |
| 0.092 | 0.057 | 0.021 | 0.049 | 0.012 |
| 0.028 | 0.021 | 0.024 | 0.029 | 0.012 |
| 0.278 | 0.143 | 0.088 | 0.149 | 0.095 |
| 0.004 | 0.005 | 0.009 | 0 | 0.022 |
| 1.463 | 1.083 | 0.921 | 0.854 | 0.801 |
| 1.783 | 1.974 | 2.268 | 2.233 | 2.192 |
| 0 | 0.001 | 0.001 | 0.004 | 0 |
| 0.062 | 0.074 | 0.040 | 0.112 | 0.150 |
| 0.005 | 0.002 | 0.009 | 0 | 0 |
| 0.001 | 0.001 | 0.001 | 0 | 0.001 |
| 7.260 | 7.126 | 7.160 | 7.158 | 7.113 |